Journal of the Mechanics and Physics of Solids 134 (2020) 103750

Contents lists available at ScienceDirect

Journal of the Mechanics and Physics of Solids

journal homepage: www.elsevier.com/locate/jmps

High-performance full-field crystal plasticity with dislocation-based hardening and slip system back-stress laws: Application to modeling deformation of dual-phase steels

Adnan Eghtesad, Marko Knezevic*

Department of Mechanical Engineering, University of New Hampshire, 33 Academic Way, Kingsbury Hall, W119, Durham, NH 03824, USA

ARTICLE INFO

Article history:
Received 25 June 2019
Revised 6 September 2019
Accepted 4 October 2019
Available online 5 October 2019

Keywords:
Microstructures
Crystal plasticity
Cyclic loading
Dual-phase steel
Parallel computing

ABSTRACT

This paper presents a microstructural cell-level crystal plasticity model aimed at predicting elasto-plastic, anisotropic, rate- and temperature-sensitive deformation of polycrystalline aggregates subjected to large plastic strains. The crystallography-based model embeds strain-path aware dislocation-based hardening and slip-system-level kinematic back-stress laws. The crystal-level response is linked to the microstructural cell-level response using an elasto-viscoplastic fast Fourier transform-based (EVPFFT) micromechanical homogenization. The overall model is ported on a high-performance computational platform integrating a graphics processing unit (GPU) to facilitate computationally efficient modeling of high-resolution microstructures. The high-performance multi-level EVPFFT is applied to modeling monotonic and cyclic deformation of dual-phase (DP) steel sheets. To this end, the effective elastic and flow stress behavior under monotonic and cyclic deformation is calculated for several steels: three DP, DP 590, DP 980, and DP 1180, and one martensitic (MS), MS 1700. Crystallographic textures and phase fractions of these steels are characterized using electron microscopy along with electron-backscattered diffraction to initialize the models. A comprehensive set of Young's modulus, Poisson's ratio, and flow stress data is used to calibrate and validate the model. The model parameters for ferrite and martensite are identified using data for two steels and used to predict the behavior of the other two streels. The model captures elasto-plastic monotonic behavior as well as the particularities pertaining to large strain cyclic deformation characteristics such as non-linear unloading upon the load reversal, the Bauschinger effect, and changes in hardening rate during strain reversals based on evolving microstructure including the evolution of dislocation density and crystallographic grain reorientation. In addition, it offers insights into the role of back-stress and dislocation annihilation on the cyclic deformation of DP steels.

1. Introduction

Advanced high strength steels (AHSS) are being developed and further improved for lighter, higher performing, and more crashworthy automobile components. Dual-phase (DP) steels belong to the AHSS class of metals. Volume fraction and dis-

* Corresponding author.
E-mail address: marko.knezevic@unh.edu (M. Knezevic).

https://doi.org/10.1016/j.jmps.2019.103750
0022-5096/

tribution of constituent martensite and ferrite phases are primary microstructural features governing mechanical properties, while the grain size and crystal lattice orientation distributions introduce secondary effects (Calcagnotto et al., 2012; Ghaei et al., 2015; Gong et al., 2016; Ma et al., 2016; Poulin et al., 2019; Woo et al., 2012). Mechanical properties such as strength and ductility can be tuned by distributing the two phases (Bhargava et al., 2018; Calcagnotto et al., 2011). Owing to the contrasting characteristics of phases, deformation behavior of DP steels is highly heterogeneous. Deformation typically starts in the large grains of ferrite, which are suitably oriented for slip (Tasan et al., 2014). Deformation can quickly localize within these large grains of ferrite. Moreover, localized deformation has been observed in channels of ferrite between bulky martensite areas. Finally, interfaces between the martensite and ferrite are also potential localization spots due to large strain incompatibilities (Jahedi et al., 2017; Kapp et al., 2011; Tasan et al., 2014; Woo et al., 2012). Thus, predicting the local and overall behavior of DP steels requires calculations of the local mechanical fields as a function of microstructure. While statistical distribution of the phases together with the local stress conditions (also determined by material internal constitution) dictates localizations, the effects are driven by applied deformation, which is often non-monotonic. One classic example of such deformation is a reverse strain path change: forward loading in the first deformation path followed by a reverse loading in the next path but in the opposite sense of direction. During load reversal, the material exhibits non-linear unloading followed by a drop in yield stress magnitude relative to that before the load reversal, i.e., the Bauschinger effect (BE) (Bauschinger, 1886; Ramazani et al., 2013; Wagoner et al., 2013; Yoshida et al., 2002, 2011; Zecevic and Knezevic, 2019). Additionally, hardening that follows during the continuation of reverse loading differs in its rate from that before the load reversal. Several physical phenomena in the material microstructure govern such behavior.

Nonlinear unloading upon load reversal originates from fractional reemission of dislocations obstructed in their glide during forward loading by dislocation substructures and interfaces such as the grain/phase boundaries (Mompiou et al., 2012; Sritharan and Chandel, 1997). The reemission process of such loosely-tangled dislocations is accompanied with the relaxation of micro back-stress arising from encountered obstacles (Sritharan and Chandel, 1997). The long-range micro back-stress fields acting against the applied stress are known as the type III stresses (Withers and Bhadeshia, 2001). During load reversal, the applied loading combines with the back-stress causing the BE (Abel, 1987; Demir and Raabe, 2010; Mughrabi, 1983; Stout and Rollett, 1990; Verma et al., 2011). Additionally, the fields of back-stress arise from the anisotropy between grains having different crystal orientations. A softer grain surrounded by harder grains will deform plastically more than its surrounding causing local incompatibility i.e. strain gradients (Bayley et al., 2006; Fleck et al., 1994). These inter-granular stresses equilibrated over a material volume are referred to as the type II stresses. These stress fields are driven by the elastic crystal properties (Verma et al., 2011). Finally, hardening rates are influenced by balancing the annihilation of the loosely-tangled dislocations formed during the forward loading and generation of new dislocations during reloading (Kitayama et al., 2013; Stout and Rollett, 1990; Wilson et al., 1990).

The present work attempts to incorporate the above summarized phenomena into a full field crystal plasticity model of an elasto-visco-plastic fast Fourier transform (EVPFFT) type in order to predict monotonic and cyclic deformation of DP steels. The model can represent spatial distribution of phases and account for grain-to-grain interactions. Thus, the model captures the inter-granular stresses of type II. The directional effects at the slip system level are incorporated using a back-stress law influencing the driving force to slip, while resistance to slip evolves based on a dislocation density-based hardening law incorporating forward and reverse dislocation density populations. As a result, the overall model is sensitive to strain paths. The model is calibrated and validated on data for several steels including DP 590, DP 980, DP 1180, and martensitic (MS) 1700 for monotonic deformation and DP 590 for large strain cyclic deformation, while demonstrating its predictive capabilities. In doing so, a unique set of model parameters is identified for ferrite and for martensite. The same set of parameters is used in the calculations for all steels. It is shown that the model can capture elasto-plastic monotonic behavior as well as the particularities pertaining to the large strain cyclic deformation for all steels. In addition, it offers insights into the role of back-stress and dislocation annihilation on the deformation behavior of DP steels. The model and these insights are presented and discussed in this paper. It is anticipated that the developed model can facilitate further understanding and optimizing microstructure of DP steels in order to achieve their higher strength, work hardening rate, ductility, and energy absorption in crash loading.

2. Modeling framework

Full-field modeling of polycrystalline metals is usually accomplished using the crystal plasticity finite element method (CPFEM) (Ardeljan et al., 2014a; Ardeljan and Knezevic, 2018; Barrett et al., 2018; Knezevic et al., 2014b), and Green's function-based elasto-visco plastic fast Fourier transform (EVPFFT) solver (Eghtesad et al., 2018a,c; Lebensohn, 2001; Lebensohn et al., 2012). The latter approach is more computationally efficient (Liu et al., 2010), especially after the recent parallel implementations of the model on central processing units (CPUs) (Eghtesad et al., 2018a) and graphics processing units (GPU) (Eghtesad et al., 2019). The latter implementation is utilized in this work and briefly summarized below. In our notation, tensors are denoted by non-italic bold letters while scalars and tensor components are italic and not bold. To denote a contracted or dot product and uncontracted or tensor product, we will use $\cdot$ and $\otimes$, respectively.

In the visco-plastic crystal plasticity framework, strain rate, $\dot{\boldsymbol{\varepsilon}}^p(\mathbf{x})$ is related to the Cauchy stress $\boldsymbol{\sigma}$ $(\mathbf{x})$ at a single-crystal material point $\mathbf{x}$ through a sum of shears on available slip systems, N (Asaro and Needleman, 1985; Hutchinson, 1976)

$$\dot{\boldsymbol{\varepsilon}}^p(\mathbf{x}) = \sum_{s=1}^{N} \mathbf{P}^s(\mathbf{x})\,\dot{\gamma}^s(\mathbf{x}) = \dot{\gamma}_0 \sum_{s=1}^{N} \mathbf{P}^s(\mathbf{x}) \left(\frac{\mathbf{P}^s(\mathbf{x}) \cdot \boldsymbol{\sigma}(\mathbf{x}) - {\tau_{bs}}^s(\mathbf{x})}{{\tau_c}^s(\mathbf{x})} \right)^n \operatorname{sgn}(\mathbf{P}^s(\mathbf{x}) \cdot \boldsymbol{\sigma}(\mathbf{x})), \tag{1}$$

where $\dot{\gamma}^s$, ${\tau_c}^s$, and $\mathbf{P}^s = \frac{1}{2}(\mathbf{b}^s \otimes \mathbf{n}^s + \mathbf{n}^s \otimes \mathbf{b}^s)$ are, respectively, the shear rate, the slip resistance and the symmetric Schmid tensor, associated with slip system (s) at a point $\mathbf{x}$. Evolution of the slip resistance term will be described later. The geometry of the slip system, s, is defined by the Burgers vector $\mathbf{b}^s$ and the unit normal $\mathbf{n}^s$. The term ${\tau_{bs}}^s(\mathbf{x})$implies the back-stress term, which will also be explained in detail shortly. Considering that the present study is concerned with body-centered cubic (BCC) structures, crystallographic slip on $\{110\}\langle\bar{1}11\rangle$ and $\{112\}\langle11\bar{1}\rangle$ systems along their 12 positive $s+$ and 12 negative s- directions will be accommodating the imposed plastic strain. Parameter $\dot{\gamma}_0$ is a reference normalization factor (taken here to be 0.001/s) and n is the power-law exponent representing the inverse of the material strain rate-sensitivity (taken here to be 20).

Hooke's law is used to represent the constitutive relation between stress and strain:

$$\boldsymbol{\sigma}^{t+\Delta t}(\mathbf{x}) = \mathbf{C}(\mathbf{x})\,\boldsymbol{\varepsilon}^{e,t+\Delta t}(\mathbf{x}) = \mathbf{C}(\mathbf{x})\left(\boldsymbol{\varepsilon}^{t+\Delta t}(\mathbf{x}) - \boldsymbol{\varepsilon}^{p,t}(\mathbf{x}) - \dot{\boldsymbol{\varepsilon}}^{p,t+\Delta t}(\mathbf{x}, \boldsymbol{\sigma}^{t+\Delta t})\Delta t\right), \tag{2}$$

where $\boldsymbol{\sigma}(\mathbf{x})$is the Cauchy stress tensor, $\mathbf{C}(\mathbf{x})$ is the elastic stiffness tensor, and $\varepsilon(\mathbf{x})$,$\varepsilon^e(\mathbf{x})$, and $\varepsilon^p(\mathbf{x})$ are the total, elastic, and plastic strain tensors. Using Eq. (2), the total strain can be defined as

$$\boldsymbol{\varepsilon}^{t+\Delta t}(\mathbf{x}) = \mathbf{C}^{-1}(\mathbf{x})\,\boldsymbol{\sigma}^{t+\Delta t}(\mathbf{x}) + \boldsymbol{\varepsilon}^{p,t}(\mathbf{x}) + \dot{\boldsymbol{\varepsilon}}^{p,t+\Delta t}\left(\mathbf{x}, \boldsymbol{\sigma}^{t+\Delta t}\right)\Delta t. \tag{3}$$

2.1. Full-field FFT homogenization

After adding and subtracting the stiffness of a reference linear medium, $\mathbf{C}^0$, from the Cauchy stress, we get

$$\sigma_{ij}(\mathbf{x}) = \sigma_{ij}(\mathbf{x}) + {C^0}_{ijkl}u_{k,l}(\mathbf{x}) - {C^0}_{ijkl}u_{k,l}(\mathbf{x}), \tag{4}$$

where $u_{k,\,l}(\mathbf{x})$ represents the displacement gradient tensor. Furthermore, we can write

$$\sigma_{ij}(\mathbf{x}) = {C^0}_{ijkl}u_{k,l}(\mathbf{x}) + \phi_{ij}(\mathbf{x}), \tag{5}$$

with

$$\phi_{ij}(\mathbf{x}) = \sigma_{ij}(\mathbf{x}) - {C^0}_{ijkl}u_{k,l}(\mathbf{x}), \tag{6}$$

where the term $\phi_{ij}(\mathbf{x})$ represents the polarization field. Using the equilibrium equation,$\sigma_{ij,j}(\mathbf{x}) = 0$, Eq. (5) becomes

$${C^0}_{ijkl}u_{k,lj}(\mathbf{x}) + \phi_{ij,j}(\mathbf{x}) = 0. \tag{7}$$

Using Green's approach for solving partial differential equations (PDEs) (Bellman and Adomian, 1985), Green's function $G_{km}(\mathbf{x})$ is associated with the displacement field $u_k(\mathbf{x})$ using

$${C^0}_{ijkl}G_{km,lj}(\mathbf{x} - \mathbf{x}') + \delta_{im}\delta(\mathbf{x} - \mathbf{x}') = 0, \tag{8}$$

and the convolution theorem (Zayed, 1998) to obtain the local displacement gradient fluctuation tensor

$$\tilde{u}_{k,l}(\mathbf{x}) = \int_{R^3} G_{ki,jl}(\mathbf{x} - \mathbf{x}')\phi_{ij}(\mathbf{x}')\,d\mathbf{x}'. \tag{9}$$

Solving Eq. (9) in Fourier space and then performing the inverse transform to get back to the real space, we can represent the strain field around the average macroscopic strain value, E_{ij}, for an infinitesimal displacement gradients using

$$\varepsilon_{ij}(\mathbf{x}) = E_{ij} + FT^{-1}\left(sym\left(\hat{\Gamma}^0_{ijkl}(\mathbf{k})\right)\hat{\phi}_{kl}(\mathbf{k})\right), \tag{10}$$

where the symbols "^" and FT^{-1} indicate direct and inverse Fourier transforms, respectively, and $\mathbf{k}$ is a point (frequency) in Fourier Space. The fourth rank tensor $\hat{\Gamma}^0_{ijkl}(\mathbf{k})$ is

$$\hat{\Gamma}^0_{ijkl}(\mathbf{k}) = -k_j k_l \hat{G}_{ik}(\mathbf{k});\ \hat{G}_{ik}(\mathbf{k}) = \left[C_{kjil}k_l k_j\right]^{-1}. \tag{11}$$

Solution of Eq. (7) necessitates an iterative procedure to obtain the stress and strain field. If we consider ${\lambda_{ij}}^{(i)}$ and ${e_{ij}}^{(i)}$to be the initial guess for the stress and strain fields, respectively, using equation Eq. (6) we have

$${\phi_{ij}}^{(i)}(\mathbf{x}) = {\lambda_{ij}}^{(i)}(\mathbf{x}) - {C^0}_{ijkl}{e_{kl}}^{(i)}(\mathbf{x}), \tag{12}$$

The next guess for the strain field is obtained using Eq. (10)

$${e_{ij}}^{(i+1)}(\mathbf{x}) = E_{ij} + FT^{-1}\left(sym\left(\hat{\Gamma}^0_{ijkl}(\mathbf{k})\right)\hat{\phi}^{(i)}_{kl}(\mathbf{k})\right). \tag{13}$$

In order to use directly the stress field rather than the polarization field, Eq. (13) can be written as (Michel et al., 2001)

$$e_{ij}{}^{(i+1)}(\mathbf{x}) = E_{ij} + FT^{-1}\left(\hat{\hat{e}}_{ij}^{(i)} + sym\left(\hat{\Gamma}^{0}_{ijkl}(\mathbf{k})\right)\hat{\lambda}_{kl}^{(i)}(\mathbf{k})\right). \tag{14}$$

An augmented Lagrangian scheme is used (Eghtesad et al., 2018a,c; Lebensohn et al., 2012) to minimize the residual as a function of the stress tensor $\boldsymbol{\sigma}^{(i+1)}$ and strain tensor$\boldsymbol{\varepsilon}^{(i+1)}$

$$R_k(\boldsymbol{\sigma}^{(i+1)}) = \sigma_k{}^{(i+1)} + C_{kl}{}^{0}\varepsilon_l{}^{(i+1)}(\boldsymbol{\sigma}^{(i+1)}) - \lambda_k{}^{(i)} - C_{kl}{}^{0}e_l{}^{(i+1)}, \tag{15}$$

In above equation the Voigt notation has been used to express the symmetric tensors σ_{ij} and C_{ijkl} as vectors of size 6

$$\begin{aligned} &\sigma_{ij} \to \sigma_k, \quad k = 1,6 \\ &C_{ijkl} \to C_{kl}, \ \ k,l = 1,6. \end{aligned} \tag{16}$$

Solving Eq. (15) using the Newton–Raphson (NR) is written as

$$\sigma_k{}^{(i+1,j+1)} = \sigma_k{}^{(i+1,j)} - \left(\frac{\partial R_k}{\partial \sigma_l}|_{\boldsymbol{\sigma}^{(i+1,j)}}\right)^{-1} R_l(\boldsymbol{\sigma}^{(i+1,j)}), \tag{17}$$

where $\sigma_k{}^{(i+1,j+1)}$ is the $(j+1)$ guess for stress field $\sigma_k{}^{(i+1)}$. Note that "j" enumerates the NR stress iterations. Coupling Eqs. (3) and (17) results in finding the Jacobian

$$\frac{\partial R_k}{\partial \sigma_l}|_{\boldsymbol{\sigma}^{(i+1,j)}} = \delta_{kl} + C_{kq}{}^{0}C_{ql}{}^{-1} + \Delta t C_{kq}{}^{0}\frac{\partial \dot{\varepsilon}_q^p}{\partial \sigma_l}|_{\boldsymbol{\sigma}^{(i+1,j)}}. \tag{18}$$

Since the slip resistance, $\tau_c{}^s(\mathbf{x})$, is a function of stress,$\tau_c{}^s(\boldsymbol{\sigma}^{(i+1,j)}(\mathbf{x}))$, the term $\frac{\partial \dot{\varepsilon}_q^p}{\partial \sigma_l}|_{\boldsymbol{\sigma}^{(i+1,j)}}$ is

$$\frac{\partial \dot{\varepsilon}_q^p}{\partial \sigma_l}|_{\boldsymbol{\sigma}^{(i+1,j)}} \cong n\dot{\gamma}_0\sum_{s=1}^{N}\frac{P^s{}_qP^s{}_l}{\tau_c{}^s\left(\boldsymbol{\sigma}^{(i+1,j)}(\mathbf{x})\right)}\left(\frac{\mathbf{P}^s(\mathbf{x})\cdot\boldsymbol{\sigma}(\mathbf{x}) - \tau_{bs}{}^s}{\tau_c{}^s\left(\boldsymbol{\sigma}^{(i+1,j)}(\mathbf{x})\right)}\right)^{n-1}. \tag{19}$$

Incorporating Eq. (19) into Eq. (18) gives

$$\frac{\partial R_k}{\partial \sigma_l}|_{\boldsymbol{\sigma}^{(i+1,j)}} \cong \delta_{kl} + C_{kq}{}^{0}C_{ql}{}^{-1} + (\Delta t\, n\,\dot{\gamma}_0)C_{kq}{}^{0}\sum_{s=1}^{N}\frac{P^s{}_qP^s{}_l}{\tau_c{}^s\left(\boldsymbol{\sigma}^{(i+1,j)}(\mathbf{x})\right)}\left(\frac{\mathbf{P}^s(\mathbf{x})\cdot\boldsymbol{\sigma}(\mathbf{x}) - \tau_{bs}{}^s}{\tau_c{}^s\left(\boldsymbol{\sigma}^{(i+1,j)}(\mathbf{x})\right)}\right)^{n-1}. \tag{20}$$

By minimizing the residual R_k by the iterative NR solver, the stress solution for each FFT sampling point is obtained as the next guess for Eqs. (12) and (14). The procedure is continued until convergence is achieved by reaching a pre-defined tolerance (TOL_{NR}) for each single crystal stress

$$\frac{\left(\sigma_k{}^{(i+1,j+1)} - \sigma_k{}^{(i+1,j)}\right)\left(\sigma_k{}^{(i+1,j+1)} - \sigma_k{}^{(i+1,j)}\right)}{\sqrt{\lambda_{ij}{}^{(i)}\lambda_{ij}{}^{(i)}}} \prec TOL_{NR} = 10^{-6} \tag{21}$$

The stress and strain field tolerance (TOL_{stress_field}, TOL_{strain_field}) after solving Eq. (15) are

$$\frac{\left\langle\left(\sigma_k{}^{(i+1)} - \lambda_k{}^{(i)}\right)\left(\sigma_k{}^{(i+1)} - \lambda_k{}^{(i)}\right)\right\rangle}{\sqrt{\frac{3}{2}\Sigma'_{ij}{}^{(i)}\Sigma'_{ij}{}^{(i)}}} \prec TOL_{stress\_field} = 10^{-6}) \tag{22a}$$

$$\frac{\left\langle\left(\varepsilon_k{}^{(i+1)} - e_k{}^{(i)}\right)\left(\varepsilon_k{}^{(i+1)} - e_k{}^{(i)}\right)\right\rangle}{\sqrt{\frac{3}{2}E_{ij}{}^{(i)}E_{ij}{}^{(i)}}} \prec TOL_{strain\_field} = 10^{-6} \tag{22b}$$

where, $\langle\rangle$ indicates volume average, while Σ_{ij} and E_{ij} denote the macroscopic stress and strain response of the homogenized polycrystal. These homogenized quantities are also calculated by taking the average of the fields over the spatial voxel-based microstructural domain using

$$\begin{aligned} &\Sigma_{ij} = \frac{\sum_{X,Y,Z}(\sigma_{ij}(\mathbf{x}))}{N^3}\ ;\ N = \#of\,voxels\,in\,X,Y,Z, \\ &E_{ij} = \frac{\sum_{X,Y,Z}(\varepsilon_{ij}(\mathbf{x}))}{N^3}. \end{aligned} \tag{23}$$

2.2. Dislocation density (DD) hardening law within EVPFFT

We incorporate a statistically stored dislocation density-based hardening law into the two-phase EVPFFT solver. In this law, the rate of dislocation storage is a thermally activated process, which is dependent on temperature and on strain rate. Versions of such hardening law have been successfully used in simulating the deformation behavior of Zr (Beyerlein and Tomé, 2008; Knezevic et al., 2014c, 2015b), Be (Knezevic et al., 2013a; Zecevic et al., 2015), Mg (Ardeljan et al., 2017, 2016; Feather et al., 2019; Lentz et al., 2015a,b), Ta (Ardeljan et al., 2014a,b, 2015a; Bhattacharyya et al., 2015; Knezevic et al., 2014a,c), an alloy of Al (Barrett and Knezevic, 2019; Zecevic and Knezevic, 2015), uranium (Ardeljan et al., 2015b; Knezevic et al., 2012, 2013b,c; Zecevic et al., 2016a,b), an alloy of Ni (Ghorbanpour et al., 2017), and a DP steel (Zecevic et al., 2016c). In our notation, superscript α implies the mode of deformation, while s and s' denote the slip systems pertaining to the mode. Evolution of slip resistance per slip system consists of

$$\tau_c^s = \tau_0^\alpha + \tau_{forest}^s + \tau_{deb}^\alpha. \tag{24}$$

The first term, τ_0^α, defines the initial slip resistance per slip mode reflecting Peierls stress and any initial population of dislocations. The second term, τ_{forest}^s, is a consequence of hardening and stands for the contribution of forest dislocations generated statistically within the microstructure with plastic deformation. The forest term is defined using the extended Taylor relationship (Kitayama et al., 2013; Zecevic et al., 2016c)

$$\tau_{for}^s = b^\alpha \chi^0 \mu^\alpha \sqrt{\rho_{tot}^s + L\sum_{s\neq s'} \rho_{tot}^{s'}}, \tag{25}$$

where, b^α represents the burgers vector of slip mode α ($2.48e-10$ m), χ^0 denotes the system interaction parameter taken to be 0.9 (Lavrentev, 1980; Mecking and Kocks, 1981). The constant L is the latent hardening parameter (set to be 1.05). The slip system shear modulus,μ^α, is obtained using the crystal compliance tensor, $\mathbf{S}(\mathbf{x})$, projected on the slip system or mode because slip systems belonging to a mode have the same shear modulus using $\frac{1}{3}(S_{44} + 4(S_{11} - S_{12} - \frac{1}{2}S_{44}))$. μ^α is calculated to be 63.07 GPa and 81.51 GPa for ferrite and martensite, using respective single crystal constants (Cantara et al., 2019). Total stored forest dislocation density is denoted with ρ_{tot}^s and its evolution is described next.

Total dislocation density is conveniently split into two dislocation populations, one termed as forward and another termed as reversible (Kitayama et al., 2013). The split facilitates introducing a deformation history dependent directionality into the hardening law. Furthermore, slip system directions whether positive or negative (i.e. $s^+,\ s^-$) on a given plane are arbitrarily assigned to the reversible dislocation population. Thus, the total dislocation density is

$$\rho_{tot}^s = \rho_{forw}^s + \rho_{rev}^{s+} + \rho_{rev}^{s-} \tag{26}$$

where ρ_{forw}^s is the dislocation density correspond to the forward loading path and $\rho_{rev}^{s+},\ \rho_{rev}^{s-}$ are reversible dislocation densities correspond to slip directions $s^+,\ s^-$, respectively.

The forward dislocation density is governed by competition between the rate of storage and the rate of dynamic recovery using (Mecking and Kocks, 1981; Zecevic et al., 2016c)

$$d\gamma^{s+} > 0 : \ \frac{\partial \rho_{forw}^s}{\partial \gamma^s} = (1-p)k_1^\alpha \sqrt{\rho_{forw}^s + \rho_{rev}^{s+}} - k_2^\alpha(\dot{\varepsilon}, T)\rho_{forw}^s, \tag{27a}$$

$$d\gamma^{s-} > 0 : \ \frac{\partial \rho_{forw}^s}{\partial \gamma^s} = (1-p)k_1^\alpha \sqrt{\rho_{forw}^s + \rho_{rev}^{s-}} - k_2^\alpha(\dot{\varepsilon}, T)\rho_{forw}^s, \tag{27b}$$

where k_1^α is a fitting constant implying the rate of generation of statistically stored dislocations. k_2^α represents the rate sensitivity coefficient related to dynamic recovery (Beyerlein and Tomé, 2008) and will be defined shortly. The parameter p will also be defined shortly. The stored reversible dislocations depend on the direction of shearing as

$$\begin{aligned} &if\ d\gamma^{s+} > 0 : \\ &\tfrac{\partial \rho_{rev}^{s+}}{\partial \gamma^s} = pk_1^\alpha \sqrt{\rho_{forw}^s + \rho_{rev}^{s+}} - k_2^\alpha(\dot{\varepsilon}, T)\rho_{rev}^{s+}, \end{aligned} \tag{28a}$$

$$\frac{\partial \rho_{rev}^{s-}}{\partial \gamma^s} = -k_1^\alpha \sqrt{\rho_{forw}^s + \rho_{rev}^{s+}} \left(\frac{\rho_{rev}^{s-}}{\rho_{tot}^s}\right)^m, \tag{28b}$$

$$\begin{aligned} &if\ d\gamma^{s-} > 0 : \\ &\tfrac{\partial \rho_{rev}^{s-}}{\partial \gamma^s} = pk_1^\alpha \sqrt{\rho_{forw}^s + \rho_{rev}^{s-}} - k_2^\alpha(\dot{\varepsilon}, T)\rho_{rev}^{s-}, \end{aligned} \tag{29a}$$

$$\begin{aligned} &\tfrac{\partial \rho_{rev}^{s+}}{\partial \gamma^s} = -k_1^\alpha \sqrt{\rho_{forw}^s + \rho_{rev}^{s-}} \left(\tfrac{\rho_{rev}^{s+}}{\rho_{tot}^s}\right)^m, \\ &with : \\ &\rho_{rev}^{s+}|_{t=0} = \rho_{rev}^{s-}|_{t=0} = 0,\ \rho_{forw}^s|_{t=0} = \rho_{initial}^s, \end{aligned} \tag{29b}$$

Table 1
Fitting parameters for the hardening law.

	Martensitic phase	Ferrite phase
τ_0^α	1100 MPa	140 MPa
k_1^α	$0.1e+08$ m^{-1}	$3.5e+08$ m^{-1}
D^α	800 MPa	550 MPa
g^α	0.019	0.015
q^α	0.1	0.1

where, the power m controls the rate of dislocation recombination and is taken here as 0.5 (Wen et al., 2015). The initial value used for the forward dislocation density population is $\rho^s_{initial} = 4.16e + 11\,\text{m}^{-2}$ for both ferrite and martensite. The parameter p indicates the shear reversibility parameter varying between 0 and 1. The reversibility parameter determines the portion of forward and reversible dislocation densities contributing to the total dislocation density. For low to moderate strain levels, $p = 1$, while for high strain levels the dislocation debris can significantly obstruct the reversible motion causing $p \le 1$ (Kitayama et al., 2013). The reversibility parameter of unity indicated that all dislocations are loosely tangled and prone to gliding in the opposite direction upon load reversal. Since the accumulated plastic strain for all simulations is the present work is relatively low (less than 0.4), a value of unity is adopted for the reversibility parameter. The parameter $k_2^\alpha(\dot{\varepsilon}, T)$ is defined as a function of absolute temperature and strain rate as follows

$$k_2^\alpha = \frac{k_1^\alpha \chi b^\alpha}{g^\alpha}\left(1 - \frac{k_B T}{D^\alpha (b^\alpha)^3} \ln\left(\frac{\dot{\varepsilon}}{\dot{\varepsilon}_0}\right)\right), \tag{30}$$

whereg^α is an effective activation enthalpy, k_B is the Boltzmann constant, $\dot{\varepsilon}_0$ is a reference strain rate taken to be $10^7\ \text{s}^{-1}$, and D^α is a drag stress. The two fitting constants are g^α and D^α.

DP steels exhibit a strong BE meaning that the dislocations formed during deformation in one direction easily annihilate upon strain reversal (Gardey et al., 2005; Wilson and Bate, 1986). Such observations have been confirmed using diffraction measurements in which shrinkage of the diffraction peak widths has been observed (Wilson and Bate, 1986). These evidences indicate that a decrease of dislocation density at strain reversal is an additional operating mechanism. Thus, in addition to the dislocation density law a small fraction of stored dislocations is removed mimicking a transient dislocation annihilation upon the load reversal.

Finally, the third term, τ^α_{deb}, is a consequence of the debris dislocation population (Madec et al., 2003) and is defined using

$$\tau^\alpha_{deb} = k_{deb}\,\mu^\alpha b^\alpha \sqrt{\rho_{deb}}\,\log\left(\frac{1}{b^\alpha \sqrt{\rho_{deb}}}\right), \tag{31}$$

where, ρ_{deb} is the debris dislocation density and $k_{deb} = 0.086$ is a material independent constant that recovers the Taylor law for low values of dislocation density. The evolution of debris dislocation density is defined as

$$d\rho_{deb} = \sum_s q^\alpha b^\alpha \sqrt{\rho_{deb}} k_2^\alpha(\dot{\varepsilon}, T)\rho^s_{tot} d\gamma^s, \tag{32}$$

Here, the evolution is coupled with the rate of dislocation recovery process. The parameter q^α is a fitting parameter separating the portion of removed dislocations ($\frac{\partial \rho^s{}_{rem,tot}}{\partial \gamma^s} = k_2^\alpha(\dot{\varepsilon}, T)\rho^s_{tot,}$) to form debris. Eq. (32) is based on thermally activated processes, such as climb and cross slip, believed to be responsible for pattern formation. These processes are mostly responsible for the recovery of forest dislocations. However, in this model, a smaller fraction of the recovered forest dislocations contribute to debris development. The debris density is used to model stage IV hardening, which manifests in large strain deformation. The fitting constants will be provided in Table 1.

2.3. Slip-system-level evolution of back-stress

The plastic deformation of DP steels starts in ferrite, while martensite remains elastic (Gong et al., 2016). The strain gradients between contrasting plastically and elastically deforming phases is accommodated by geometrically necessary dislocations (GNDs), which are sources of localized hardening and back-stress fields (Nesterova et al., 2015). Moreover, measurements also show that the properties of the ferrite phase change with distance from the martensite grains i.e. the grains of the ferrite phase are harder in the vicinity of martensite grains (Kadkhodapour et al., 2011). The variation stems from the volume expansion strains created during austenite-martensite transformation, which are accommodated primarily by GNDs (Sakaki et al., 1983). Thus, the stress fields in the ferrite phase around martensite will vary with the distance from the martensite phase. Additional back-stress fields arise from dislocation debris surrounded by GNDs (stress type III), primarily in the ferrite phase (Mughrabi, 2001). As a result, back-stress fields are present locally in both ferrite and martensite phases, while these stress fields vanish at the volume average sample level (Brown and Stobbs, 1971). Strain gradients of plastic slip govern the GND density and then the GND density governs back-stress field (Evers et al., 2004). Such strain gradient

Table 2
Fitting parameters for the back-stress law.

	Martensitic/ferrite phase
ν	200
A_{bs}	3.0
γ_b	0.01
τ_{bs}^{sat}	25 MPa

plasticity formulations have been developed within the full-field crystal plasticity solvers (Evers et al., 2004; Lebensohn and Needleman, 2016). However, due to significant difficulties with such formulations, a phenomenological approach is adopted here to approximate the evolution of back-stress fields. Since the GNDs are not considered by the model, the back-stress evolves with plastic strain per crystal giving rise to the kinematic hardening effects. While the adopted approach is a gross simplification of the actual physical phenomena, it is relatively simple and computationally efficient. While the stress field around GNDs is tensorial (Bayley et al., 2006), only the resolved stress component on a gliding slip system enters our back-stress definition (Evers et al., 2004; Kim et al., 2012). Such formulation is known as self-internal back-stress formulation (Bayley et al., 2006). In our work, the same formulation is used for ferrite and martensite, which is another simplification since the effects of the fields are likely not the same for the two phases.

The evolution law for the slip system level micro back-stress helping or hindering the deformation in ferrite and martensite consists of the following equations given an increment in shear $d\gamma^{s+/-} > 0$ (whether in the forward + or in the reverse – direction) (Zecevic et al., 2016c)

$$\begin{aligned} & if\ \ \tau_{bs,sys}^{s+/-} > 0: \\ \overset{*}{\gamma}{}^{s+/-} &= \frac{-1}{\nu}\ln\left(1-\frac{\tau_{bs,sys}^{s+/-}}{\tau_{bs}^{sat}}\right), \end{aligned} \tag{33a}$$

$$\begin{aligned} \tau_{bs,sys}^{s+/-} &= \tau_{bs}^{sat}\left(1-\exp\left(-\nu\left(\overset{*}{\gamma}{}^{s+/-}+d\gamma^{s+/-}\right)\right)\right), \\ \tau_{bs,sys}^{s-/+} &= -A_{bs}\tau_{bs,sys}^{s+/-}, \end{aligned} \tag{33b}$$

$$\begin{aligned} & elseif\ \ \tau_{bs,sys}^{s+/-} < 0: \\ \overset{**}{\gamma}{}^{s+/-} &= -\gamma_b\ln\left(\frac{\tau_{bs}^{sat}-\tau_{bs,sys}^{s+/-}}{(A_{bs}+1)\tau_{bs}^{sat}}\right), \end{aligned} \tag{33c}$$

$$\begin{aligned} \tau_{bs,sys}^{s+/-} &= -(A_{bs}+1)\tau_{bs,sys}^{s+/-}\exp\left(-\frac{\overset{**}{\gamma}{}^{s+/-}+d\gamma^{s+/-}}{\gamma_b}\right)+\tau_{bs}^{sat}, \\ \tau_{bs,sys}^{s-/+} &= -\frac{1}{A_{bs}}\tau_{bs,sys}^{s+/-}, \end{aligned} \tag{33d}$$

where $\tau_{bs,sys}^{s+/-}$ is the slip system level back-stress for the two opposite directions, s^+ and s^-. A_{bs} and ν are the back-stress fitting parameters. The parameter A_{bs} can promote asymmetry in the evolution of back-stress between two opposite slip directions to better capture micro-back-stresses present in dislocation pile-ups, which are responsible for non-linear unloading upon load reversal (Sritharan and Chandel, 1997). The cut-off limit at which the back-stress evolution will saturate τ_{bs}^{sat} is also a fitting parameter. As is evident, for back-stress to evolve in a grain, the grain must deform plastically to an accumulated magnitude of shear $\gamma^{s+/-}$. The back-stress fitting parameters will provided in Table 2.

The above described slip system kinematic hardening effects are suitably defined to capture the local plasticity processes responsible for nonlinear unloading and the BE. While $\tau_{bs}^{s^+}$ acts in the direction opposite to the driving force on s^+, i.e. $\mathbf{P}^{s^+}\cdot\boldsymbol{\sigma}-\tau_{bs}^{s^+}=\tau_c^s$, meaning that $\tau_{bs}^{s^+}$ lowers the driving force, $\tau_{bs}^{s^-}$ aids the driving force on the slip system s^- according to: $\mathbf{P}^{s^-}\cdot\boldsymbol{\sigma}-\tau_{bs}^{s^-}=\tau_c^s$.

2.4. High performance EVPFFT

Running EVPFFT simulations involving multi-phase materials, which require high resolutions of at least 64^3, especially for cyclic loading, is computationally challenging. In our recent work, we have developed a GPU accelerated version of the model, termed ACC-EVPCUFFT (Eghtesad et al., 2019) to facilitate computationally efficient simulations using EVPFFT. The need for computationally efficient codes for crystal plasticity modeling has been highlighted in several studies (Barrett et al., 2019; Barton et al., 2011; Knezevic and Savage, 2014; Savage and Knezevic, 2015). The version takes advantages of the OpenACC standard and CUFFT library. The version is utilized in the present work and, for the first time, run on the latest NVIDIA Tesla V100 graphics card. Fig. 1 shows the performance benchmark of ACC-EVPCUFFT code running on NVIDIA Tesla V100 device relative to the original scalar version of the code. Furthermore, the figure shows that the ACC-EVPCUFFT model

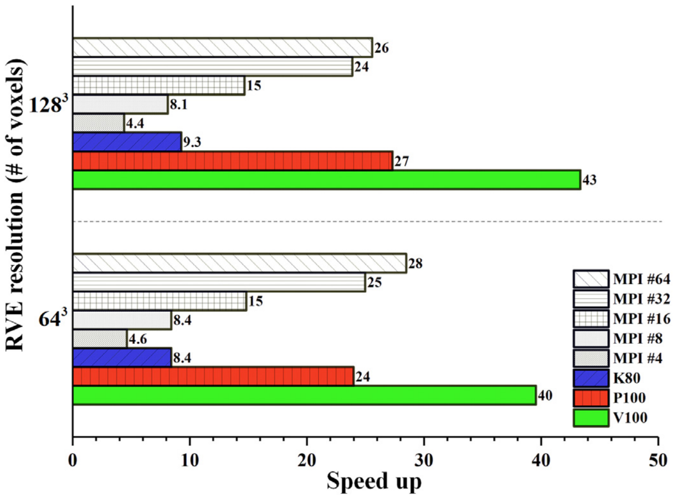

Fig. 1. Performance benchmark using MPI-EVPFFT (Eghtesad et al., 2018a) and ACC-EVPCUFFT (Eghtesad et al., 2019) parallel implementations enhanced in this work for the dislocation-based hardening and backstress laws for two RVE domain sizes (i.e. voxel resolutions). The MPI version of the code is run on 4, 8, 16, 32, and 64 processes while the GPU versions are run on Nvidia Tesla K80, P100, and V100 GPUs. The speed up is normlaized over the original scalar version of the code (Lebensohn et al., 2012), which utilizes the FOURN routine while the MPI-EVPFFT and ACC-EVPCUFFT use the MPI-FFTW and CUFFT, respectively, for the FFT calculations.

is not only substantially faster from the original code but also from the MPI-EVPFFT (Massage Passing Interface) version exercised up to 64 CPUs. The MPI-EVPFFT was developed in (Eghtesad et al., 2018a). The figure also shows the acceleration obtained using older version of the GPU cards, K80 and P100. All simulations presented in this paper were run on CPU cores of Intel Xeon 2695 v4.

3. Results

This section uses the ACC-EVPCUFFT model enhanced for the DD hardening and back-stress laws to simulations deformation behavior of DP steels.

3.1. Microstructure of DP590, DP980, DP1180, and MS1700

Microstructure formation and phase partitioning in DP steels depends on the synthesis and processing routes (Rocha et al., 2005; Schemmann et al., 2015). DP steels studied in the present work have been acquired as rolled sheets from US Steel. DP 590, DP 780, and DP 980 are from US Steels' hot dip (HD) processing lines, while DP1180 is from their continuous annealing line (CAL). DP 590 and DP 780 were galvannealed (HDGA) coated, DP 980 was galvanized (HDGI) coated, and DP 1180 was bare. The grades of the commercial DP steel are designated by their ultimate tensile strength (UTS) in MPa. The sheet thicknesses were 1.3, 1.4, 1, and 1 mm for DP 590, DP 780, and both DP 980 and DP 1180 respectively. The studied steels are typical of auto-body/structure applications. In order to simulate their deformation behavior using the ACC-EVPCUFFT model, numerical simulation setups in terms of voxel-based microstructural cells i.e. representative volume elements (RVEs) are first synthetically constructed. In these setups, grain structure, volume fraction of phases, texture, and misorientation distribution for each phase are considered as microstructural features governing the local and overall deformations behavior of the steels. The microstructures are generated using the DREAM3D software package (Groeber and Jackson, 2014) and shown in Fig. 2. The grain structure and texture are based on the EBSD scans, while phase volume fractions are primarily based on scanning electron microscopy (SEM) images (Cantara et al., 2019; Knezevic and Landry, 2015; Zecevic et al., 2016c). Every microstructural cell consist of 256^3 voxels embedding several thousand grains. The voxelized data consists of voxel coordinates, grain IDs, phase IDs, and crystal orientation for every FFT point (i.e. voxel) of the call. The cell for DP 590 embeds 1218 grains for ferrite and 6051 grains for martensite. The cell for DP 980 embeds 11,803 grains for ferrite and 6365 grains for martensite. The cell for DP 1180 embeds 6005 grains for ferrite and 4079 grains for martensite. The cell for MS 1700 embeds 1054 grains for ferrite and 7969 grains for martensite. The measured textures for each steel were loaded in DREAM3D and assigned to ferrite, while a uniform random texture is assigned to martensite. Stereographic pole figures visualizing ferrite textures for each steel are shown in Fig. 3 (Cantara et al., 2019; Eghtesad et al., 2018b; Zecevic et al., 2016c). The pole figures are plotted with the EDAX orientation imaging microscopy (OIM) analysis software from TexSEM Laboratories (TSL) (EDAX and TSL). As is evident, the steel sheets have typical orthotropic rolled texture of BCC metals, where a majority of the grains are oriented around the γ-fiber and a portion of the α-fiber (Bunge, 1993; Jahedi et al., 2014; Knezevic et al., 2014c, 2015a; Kocks et al., 1998; Lücke and Hölscher, 1991; Randle and Engler, 2000; Ray et al., 1994; Smith et al., 2016; Von Schlippenbach et al., 1986; Zecevic and Knezevic, 2018b). We have attempted to

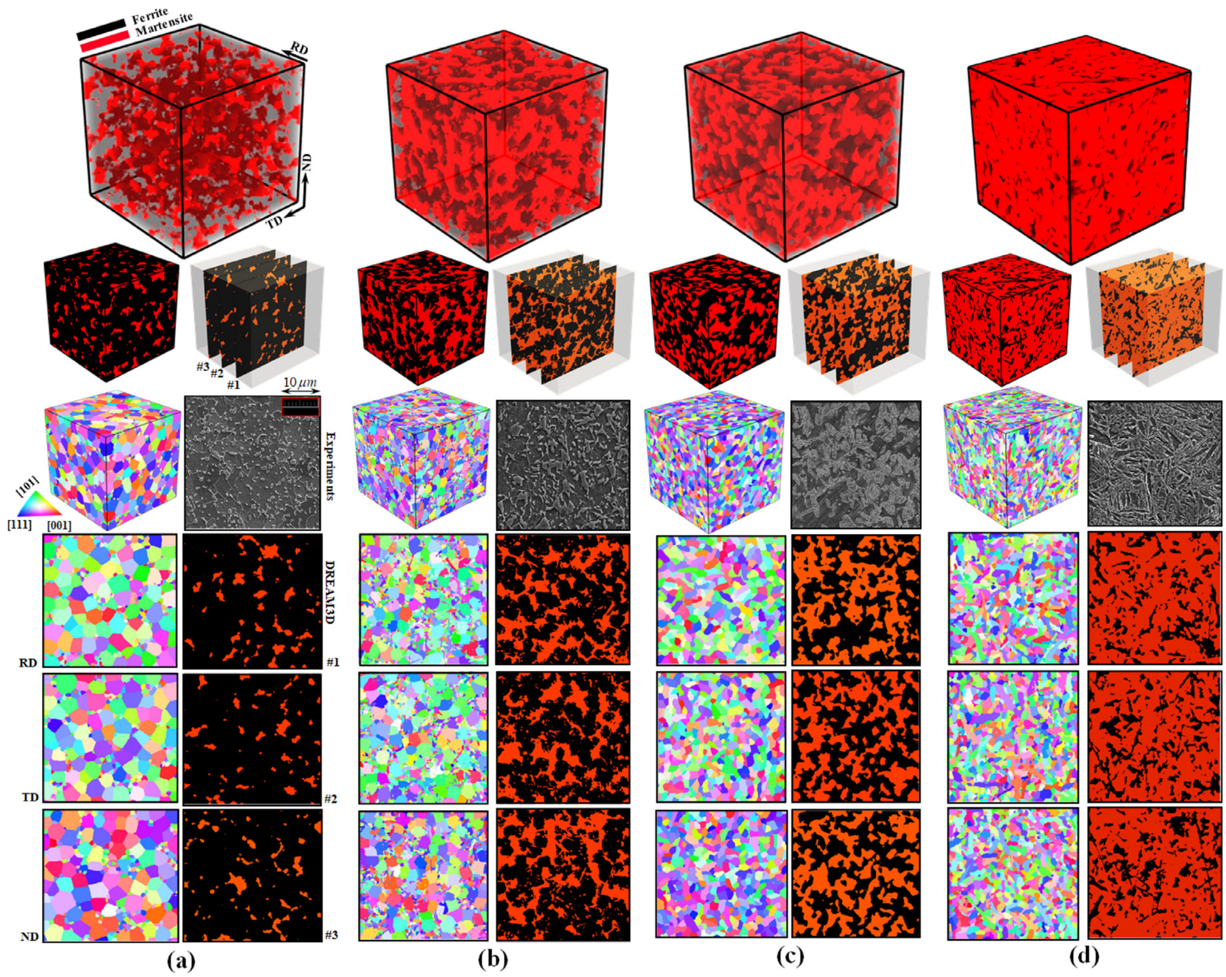

Fig. 2. Microstructural cells for (a) DP 590 (b) DP 980 (c) DP 1180 and (d) MS 1700 steels generated in DREAM.3D based on statistical input in terms of orientation distribution function and phase fraction. The first row from top indicates the volume rendering of martensite (red) illustrating its distributions. The second row shows the surface of the cells along with several slices in RD direction revealing internal phase distribution. The third row represents the inverse pole figure (IPF) maps and further compares the phase distribution with secondary electron (SE) images. The labeling in (a) applies to (b), (c) and (d).

separate the texture of the martensitic phase in each steel and obtained these to be weak (i.e. approximately random). Thus, texture of the martensitic phase is assumed as uniform random. The phase fraction estimates for martensite are 7.7%, 39%, 45%, and 80% for DP 590, DP 980, DP 1180, and MS 1700, respectively. With increasing volume fraction of martensitic, the phase distribution in the cells evolves from small islands surrou nding ferrite to larger connected regions of martensite. While different microstructural topologies govern local mechanical fields as highlighted in (Berbenni et al., 2004; Tasan et al., 2015, 2014), the overall homogenized stress–strain response is similar given the phase fractions, grain shape/size, and texture.

In order to ensure the RVE domains are of sufficient resolution, we performed a resolution sensitivity study with resolutions of $16^3, 32^3, 64^3, 128^3, 256^3$. Fig. 4 presents results of the study for macroscopic stress–strain response of DP1180 steel. The convergence in terms of the macroscopic response is obtained with 128^3, meaning that increasing the resolution does not change the results. However, we adopt the resolution of 256^3 for all simulations to better represent the micromechanical fields, especially those at interfaces.

3.2. Model calibration and validation

In this section, the ACC-EVPCUFFT model is first verified for predicting elastic anisotropy and then adjusted for predicting the plasticity of DP steel sheets.

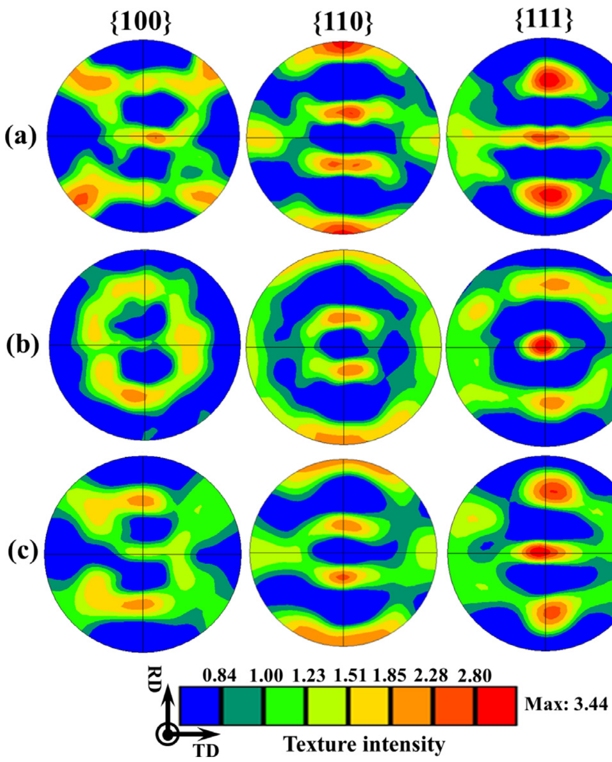

Fig. 3. Stereographic pole figures measured by EBSD showing initial texture for: (a) DP 590, (b) DP 980, and (c) DP 1180.

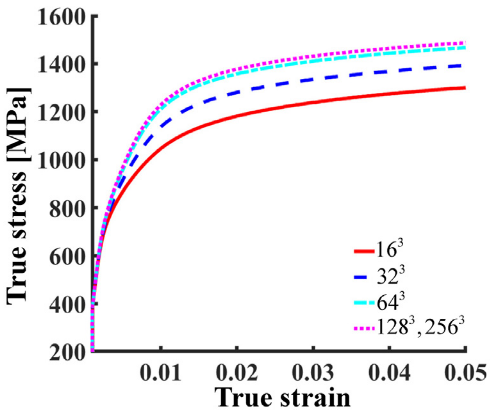

Fig. 4. Calculated true stress-true strain response of DP 1180 as a function of microstructural cell resolution to evaluate the convergence of the EVPFFT solver for macroscopic response.

3.2.1. Elastic properties

After a metallic part is removed from a forming die, the mechanical fields evolve to a new equilibrium, which is accompanied by geometrical changes (springback). Such dimensional changes are largely driven by elastic properties. Thus, a constitutive model used in predicting springback in metal forming should consider elastic anisotropy, as highlighted in (Sumikawa et al., 2016; Wagoner et al., 2013). In our recent work, we have studied elastic response of DP steels based on the self-consistent homogenization method (Cantara et al., 2019). In doing so, we have estimated the single crystal elastic stiffness coefficients for martensite and ferrite by predicting the orientation dependent Young's modulus and Poisson's ratio data reported in Deng and Korkolis (2018). The estimated crystal constants are $C_{11} = 218.37$ *GPa*, $C_{12} = 113.31$ *GPa*, $C_{44} = 105.34$ *GPa* for ferrite and $C_{11} = 282.31$ GPa, $C_{12} = 116.19$ GPa, $C_{44} = 78.57$ GPa for martensite. Estimates of the effective elastic properties of a polycrystal depend on microstructure, accuracy of available single crystal constants, and selected homogenization procedure linking the crystal to the overall effective elastic response. Here, we run the ACC-EVPCUFFT full-field homogenization with the same crystal constants for the given microstructural cells (Fig. 2) to evaluate whether the

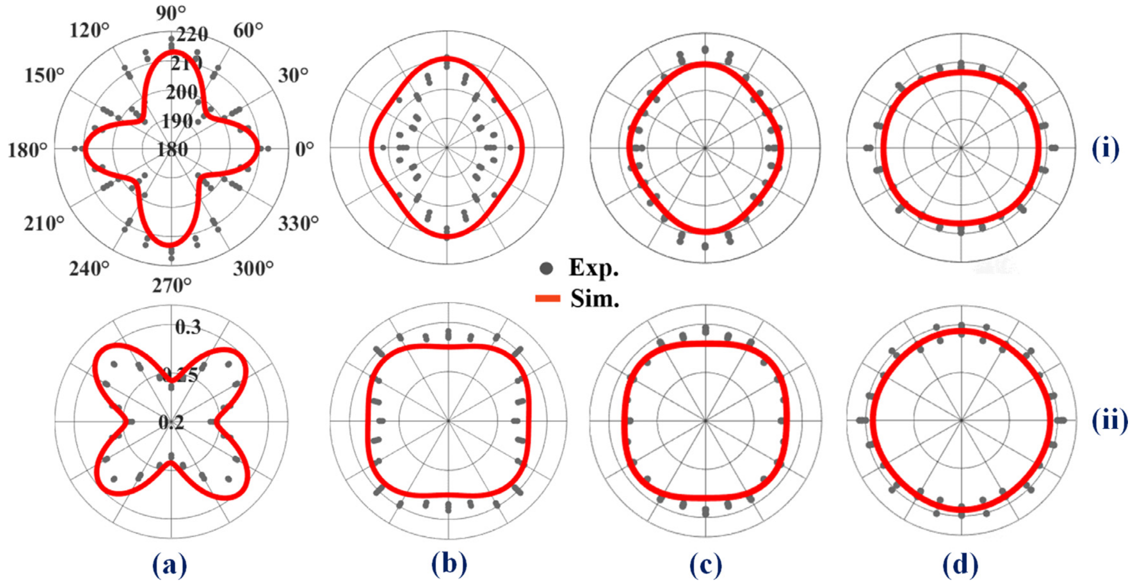

Fig. 5. Comparison of measured and predicted variation of effective Young's modulus (top row) and Poisson's ratio (bottom row) with the in-plane sheet orientation for: (a) DP 590, (b) DP 980, (c) DP 1180, and (d) MS 1700. The angle starts from the rolling direction (i.e. 0° = RD).

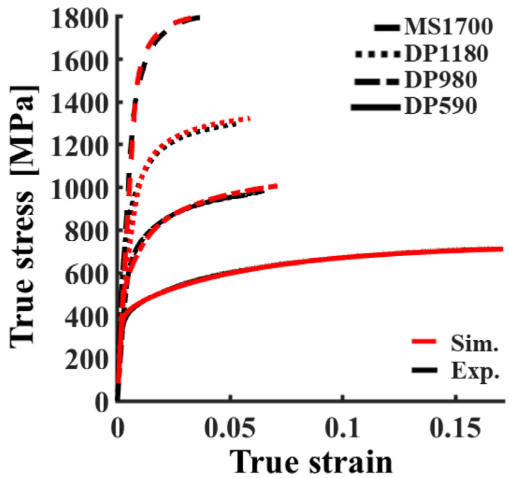

Fig. 6. Comparison of measured and calculated true stress-true strain response for: DP 590, DP 980, DP 1180, and MS 1700 steels under simple tension.

model will predict the orientation dependent data. Fig. 5 shows the results demonstrating a good agreement between the calculations and the data. These results are regarded as predictions because of no model calibration. The polar plots show the evolution of Young's modulus and Poisson's ratio anisotropy from DP590 (large) to MS1700 (small), which is a consequence of crystal constants and microstructure. Good predictions of local and overall anisotropic elastic response is essential for estimating the distribution of elastic back-stress fields in the material (Hasegawa et al., 1975), which will be exploited shortly for studying the elasto-plastic response of these steels during their large strain cyclic deformation.

3.2.2. Hardening behavior

The model is used to simulate first monotonic deformation of DP 590, DP 980, DP 1180, and MS 1700 and then cyclic tension-compression-tension deformation of DP 590 steel. Consistent with experiments, the simulations are performed under an applied strain rate of 0.001 s^{-1} at room temperature (298 K). Simple tension/compression boundary conditions are imposed along a loading direction, while enforcing zero average stress along the two lateral directions of the RVEs. This is facilitated by applying a mixed Cauchy stress and strain rate boundary conditions in the EVPFFT model. Monotonic experimental data for DP 590 and DP 1180 are used for model calibration, while the rest for model validation. Likewise, part of cyclic data is used for model calibration, while the rest for model validation. In order to capture the monotonic

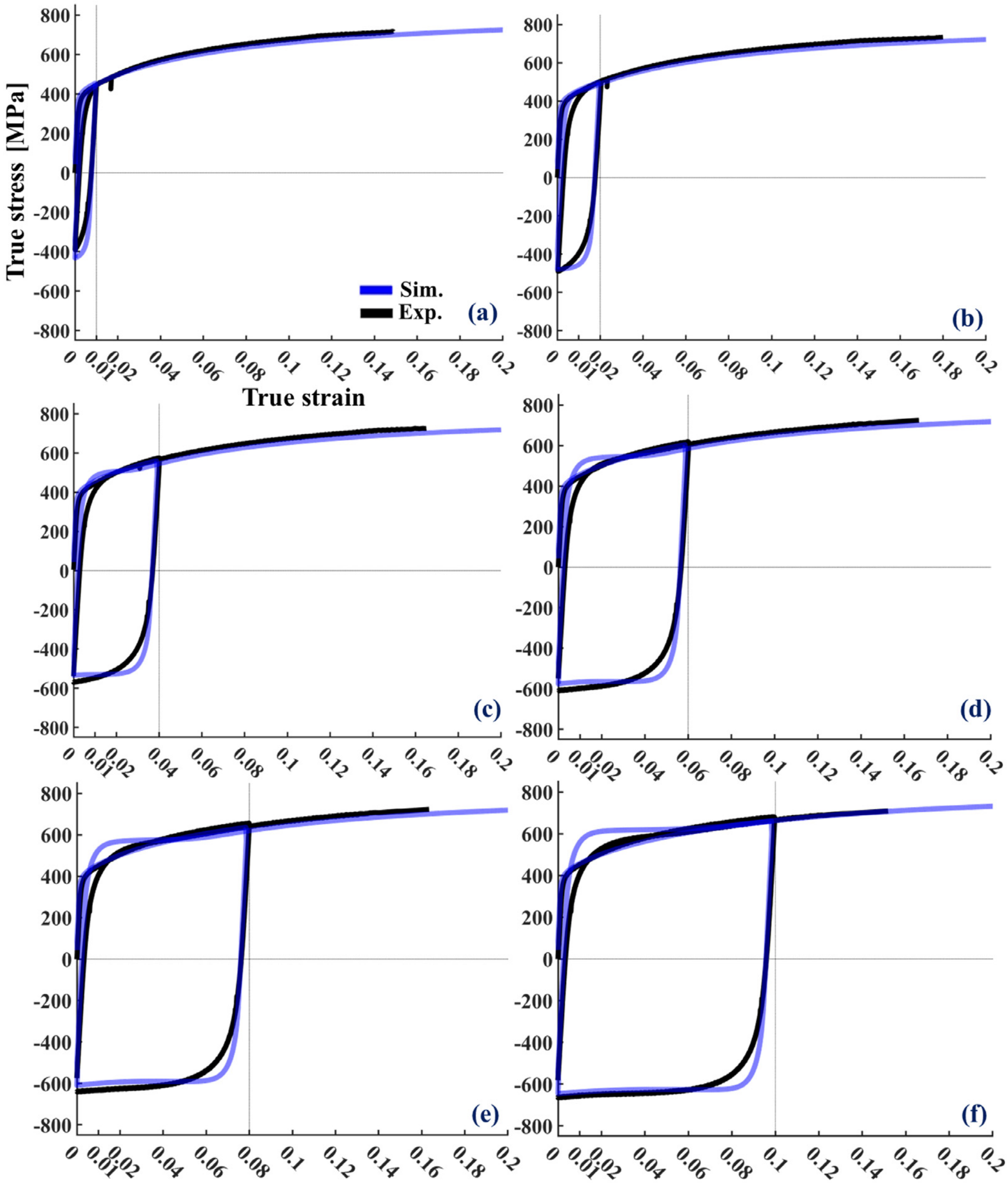

Fig. 7. Comparison of measured and calculated (without accounting for backstress) true stress-true strain cyclic (tension–compression to zero strain–tension to failure) response along RD with the following pre-strain levels in tension: (a) 0.01 (b) 0.02 (c) 0.04 (d) 0.06 (e) 0.08 (f) 0.10 for DP 590. The reversible dislocation density was modeled.

response, the following parameters associated with the hardening laws are fit for ferrite and martensite: initial slip resistance, τ_0^α, trapping rate coefficient, k_1^α, activation barrier for de-pinning, g^α, drag stress, D^α, and the rate coefficient q^α. The fitting procedure starts with varying τ_0^α to fit yield stress. Next, k_1^α, is adjusted such that the initial hardening slope is reproduced. Next, g^α and D^α are adjusted to match the hardening behavior. Finally, q^α is adjusted to capture the later stage of the hardening behavior. In order to capture the cyclic response, the following back-stress law parameters are fit: saturation value for back-stresses τ_{bs}^{sat}, asymmetry factor, A, and parameters ν and γ_b. Here, both τ_{bs}^{sat} and A are adjusted simultaneously to obtain the asymmetric yield and non-linear unloading upon load reversal. Once this is achieved, tuning ν and γ_b simply provides more accurate fits. The hardening and back-stress parameters are given in Tables 1 and 2, respectively.

Fig. 6 shows results of the calculations for the four DP steels based on a single set of parameters for ferrite and a single set of parameters for martensite. The only variable in the calculations controlling the response is the initial microstructure

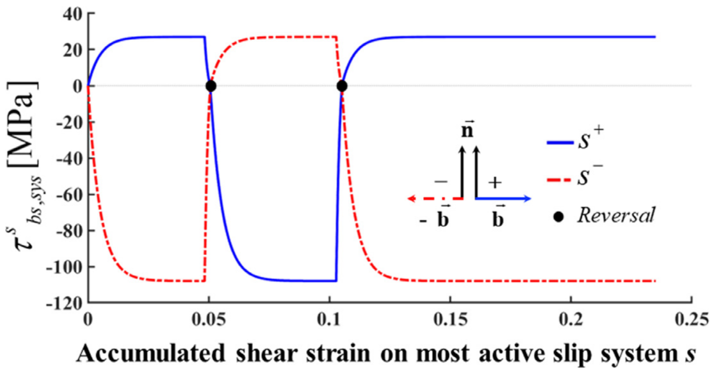

Fig. 8. Magnitude of backstress with accumulated shear strain in a randomly selected ferrite grain for the sth slip system with highest activity during the forward tension and the 1st and the 2nd reversal.

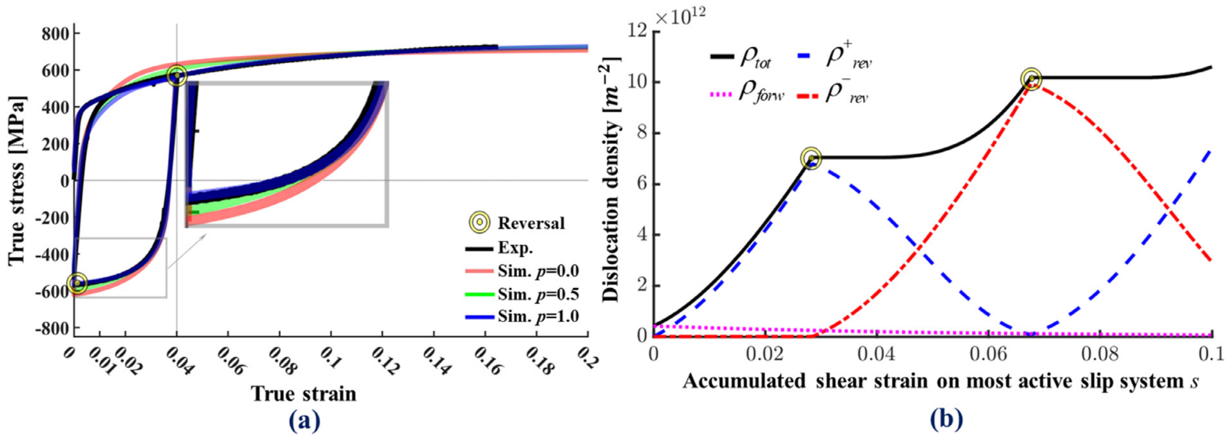

Fig. 9. (a) Effect of reversible dislocation population driven by the reversibility parameter ($0 \leq p \leq 1$) on hardening during loading in the reverse direction. (b) Evolution of dislocation populations for $p = 1$ up to an accumulated shear of 0.1 for a slip system with the highest activity in a randomly selected ferrite grain.

(Fig. 2). After successful predictions of the monotonic loading conditions, we run large strain cyclic tension-compression-tension simulations. Here, active slip systems experience at least two reversals in shearing direction.

To show the effect of back-stress, Fig. 7 shows the comparison between simulated and experimental curves without accounting for back-stress in the simulations. As is evident, the BE is not predicted well. Fig. 8 shows typical predictions of back-stress evolution on a slip system influencing magnitude of the resolved shear stress. Next, we show the effect of reversible dislocation population, which is driven by the reversibility parameter ($0 \leq p \leq 1$). Increasing the reversibility parameter decreases the hardening rate mimicking the easy motion and annihilation of loosely tangled dislocations in the opposite direction. The implementation addresses the issue of over-estimation of the hardening after the second reversal and right before the last monotonic loading step. The red line in Fig. 9a shows this over-shooting which happens when no reversible dislocations are considered (i.e.$p = 0$), while the blue line shows the complete reversible implementation (i.e.$p = 1$). Fig. 9a shows that the value of $p = 1$ is the most appropriate for the studied pre-strain levels. Fig. 9b represents a typical evolution of total (ρ_{tot}) and reversible dislocation densities (ρ^{s+}_{rev}, ρ^{s-}_{rev}) with accumulated shear strain on a slip system. Fig. 10 shows the predictions after accounting for both effects (back-stress and reversible dislocations). It can be seen that the model is capable of capturing all features particular to the cyclic behavior of DP 590. Importantly, the model predictions are based on a single set of fitting parameters.

4. Discussion

This work has integrated a strain path sensitive dislocation density-based hardening law, a back-stress law, and intrinsic inter-granular backstress along with crystal elastic anisotropy within a full-field ACC-EVPCUFFT crystal plasticity solver to enable predictions of the macroscopic deformation behavior of DP steels. The novel feature of the model capturing underlying mechanisms of plastic deformation facilitated good predictions of the monotonic and cyclic response of

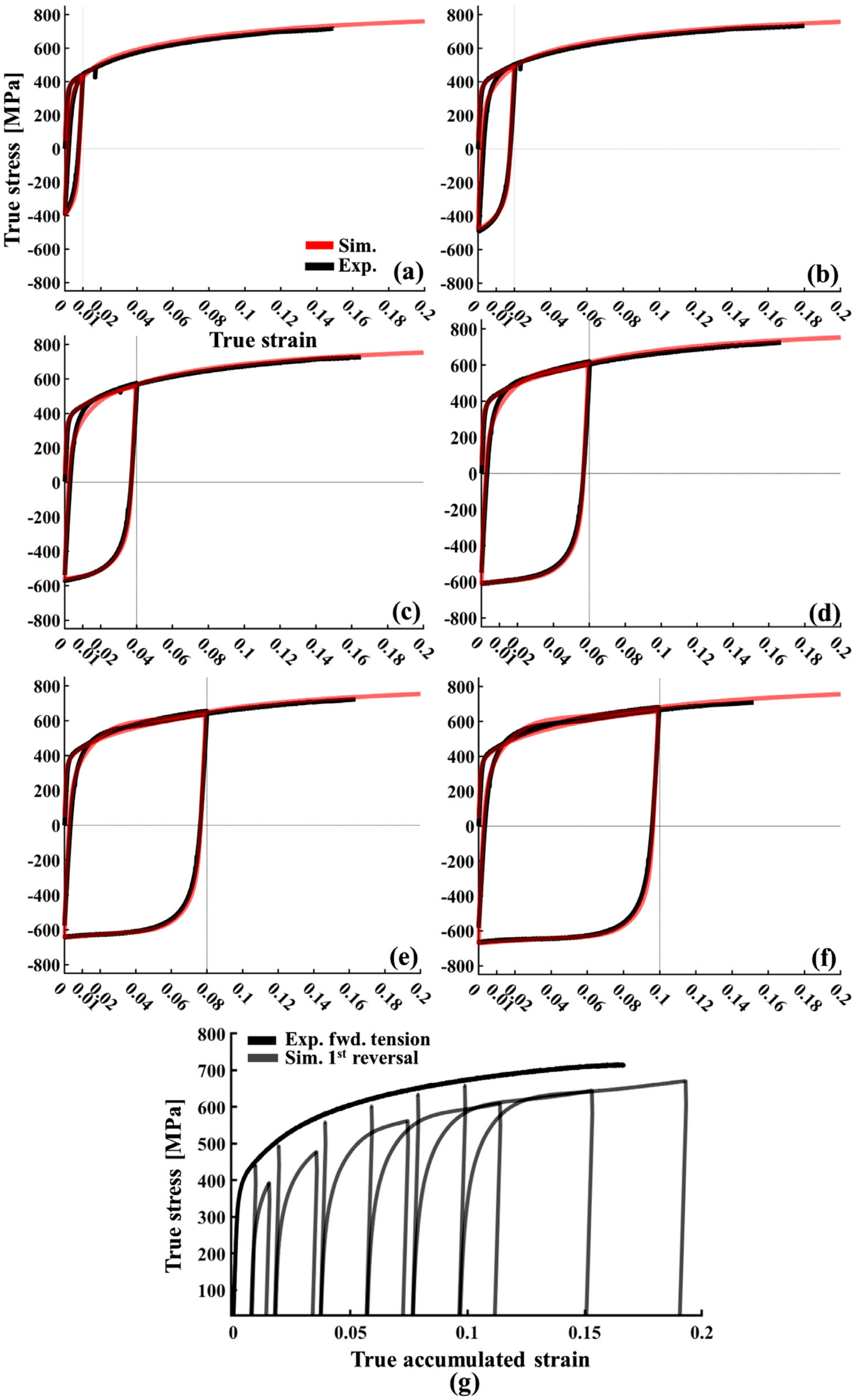

Fig. 10. Comparison of measured and calculated (after accounting for backstress and reversible dislocations) true stress-true strain cyclic (tension–compression to zero strain–tension to failure) response along RD with the following pre-strain levels in tension: (a) 0.01 (b) 0.02 (c) 0.04 (d) 0.06 (e) 0.08 (f) 0.10 for DP 590. (g) Forward and the 1st reversal curves as a function of accumulated true strain showing drops in yield stress i.e. the permanent softening upon load reversal.

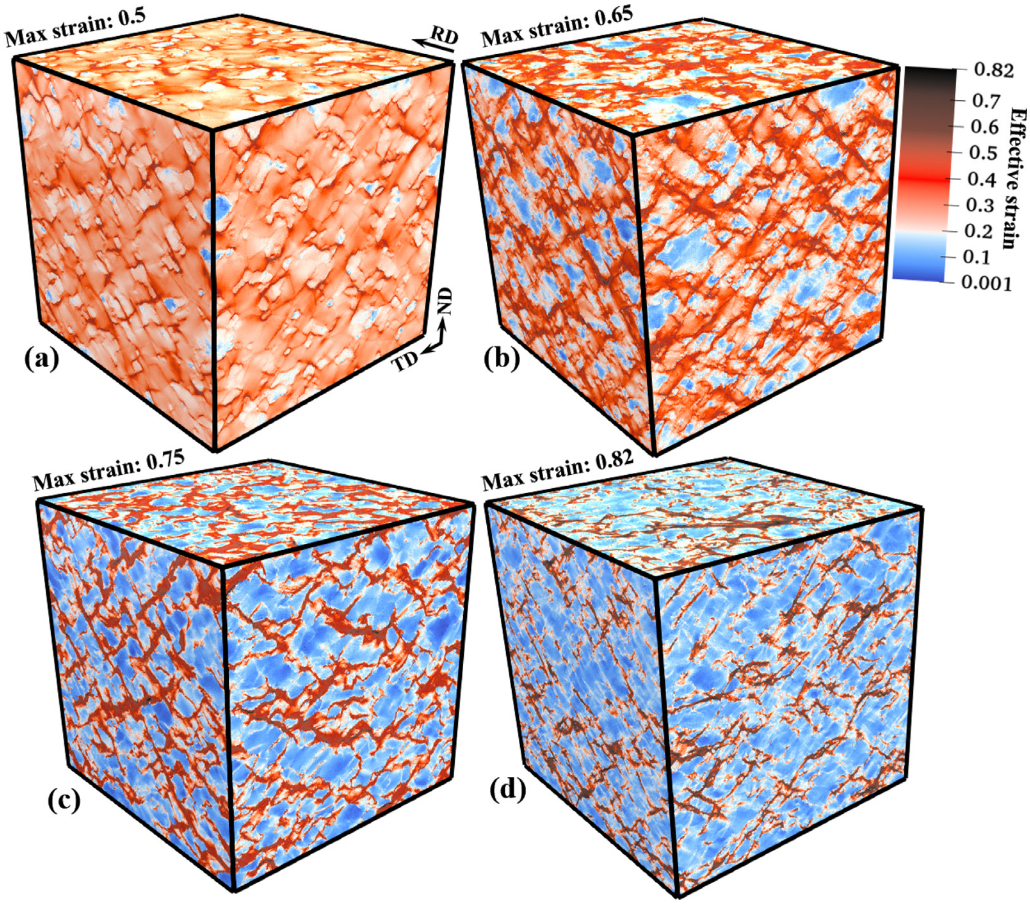

Fig. 11. Fields of effective plastic strain over a microstructural cell for: (a) DP 590, (b) DP 980, (c) DP 1180, and (d) MS 1700. The cells were consistently deformed to a strain of 0.035 (i.e. the uniform elongation strain for MS1700 sample).

DP steels. The individual contributions of back-stress and reverse dislocation motion have been illustrated in Figs. 7 and 9. Clearly, both the evolution of back-stress and the annihilation of dislocation densities are important mechanisms for accurate predictions of deformation behavior of DP steels. The predicted flat regions in Fig. 9b reveal that upon a strain reversal some deformation can be accommodated without a substantial increase in dislocation density. Such results are in agreement with assumption made in several other cyclic plasticity constitutive models (Ohno, 1982; Ohno and Kachi, 1986; Zecevic and Knezevic, 2018a).

While the scope of the modeling presented in this paper was primarily to predict the macroscopic behavior as a function of microstructural features considering the phase fractions as the most dominant feature, in closing we discuss the predicted mechanical fields over microstructural cells. Fig. 11 shows fields of the effective plastic strain, while Fig. 12 depicts fields of von Mises stress at given strain levels for the studied steels. The ability to predict such fields is an advantage of full-field models such as ACC-EVPCUFFT over mean-filed approaches. Owing to contrasting strength characteristics between ferrite and martensite, highly heterogeneous fields can be observed. Grains of martensite develop much larger stress than grains of ferrite, while the amount of plastic strain is significantly lower in these grains than those of ferrite resulting in large gradients, as revealed in the figures. Due to a large fraction of ferrite, the deformation of DP 590 is the most homogeneous amongst the studied steels. Deformation starts in large regions of ferrite, while martensite is steel elastic. After substantial deformation of the ferrite phase deforms, the martensite phase yields. By that time, channels of highly deformed ferrite between bulky martensite areas have developed. The effect is larger in the steel with smaller amount of ferrite. With increasing the volume fraction of martensite, the gradients sharpen narrowing the high strain bands and reducing the overall ductility. Beyond predicting stress and strain field localizations, future work will advance the model to predict damage accumulation in grains and at interfaces as a function of microstructural topology. A similar study into the partitioning of mechanical fields in a measured 3D microstructure of a DP steel has been carried out using a phenomenological crystal plasticity model and a spectral method approach implemented in the Düsseldorf Advanced Material Simulation Kit (DAMASK) (Diehl et al., 2017). In particular, the study revealed the importance of modeling full 3D microstructures as opposed to 2D microstructures. While no large effect on the global response were found, 2D modeling of the local stress and strain fields differed quantitatively

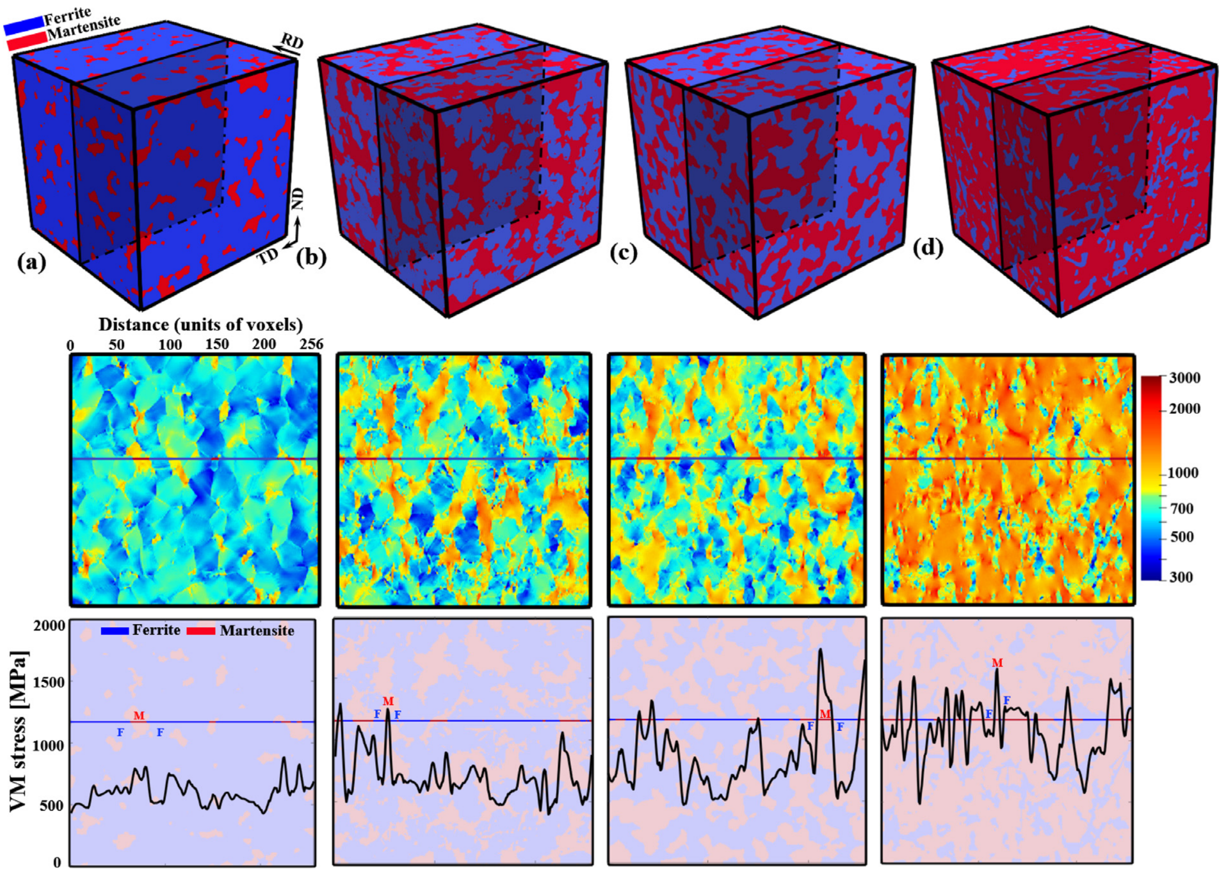

Fig. 12. Fields of von Mises (VM) stress over a microstructural cell section for: (a) DP 590, (b) DP 980, (c) DP 1180, and (d) MS 1700DP. The cells were deformed to a strain of 0.005.

and qualitatively from modeling in 3D, rendering the 2D models not suitable, especially for simulations tackling the damage initiation in DP steels.

5. Conclusions

This paper develops a comprehensive full-field polycrystal plasticity model capable of predicting monotonic and cyclic elasto-plastic deformation of DP steels deforming by crystallographic slip. Specifically, a dislocation density-based hardening law and a slip system level back-stress kinematic hardening law are implemented into the ACC-EVPCUFFT micromechanical model making the overall formulation as strain-path sensitive. The model is capable of taking advantage of high-performance computational platforms integrating GPU cards to facilitate computationally efficient modeling. The dislocation law facilitates annihilation of dislocation populations to capture the experimentally observed reduction of dislocations after strain reversals. While the annihilation of dislocations is important for predicting the BE and the changes in the hardening rates during reverse loading, the back-stress in conjunction with the elastic anisotropy primarily controls the non-linear unloading and also influences the BE. The developed model is calibrated and validated on mechanical data for DP 590, DP 980, DP 1180, and MS 1700 steels sheets. Crystallographic textures and phase fractions of these steels are characterized using electron microscopy along with electron-backscattered diffraction. Based on the data, microstructural cells are constructed for each steel in DREAM3D. The model parameters for ferrite and martensite are identified using the cells for two steels and then used to predict the behavior of the other two streels. The model is shown to capture elasto-plastic monotonic behavior as well as peculiarities pertaining to large strain cyclic deformation characteristics such as non-linear unloading upon the load reversal, the BE, and changes in hardening rate during strain reversals based on evolving microstructure including the evolution of dislocation density and crystallographic grain reorientation. Significantly, the predictions for the four steels with varying content of martensite are based on a single set of parameters, one for ferrite and another for martensite. Since full-field, the model offers insights into the development of highly heterogeneous mechanical fields because of contrasting strength characteristics between constituent phases. Channels of highly deformed ferrite regions between bulky martensite areas are predicted limiting the elongation of steels, especially those with high content of martensite. Future work will focus on incorporating the ACC-EVPCUFFT model into the finite element method tools to facilitate applying boundary conditions for metal forming simulations.

Acknowledgments

This research is sponsored by the U.S. National Science Foundation, accomplished under the CAREER grant no. CMMI-1650641.

Supplementary materials

Supplementary material associated with this article can be found, in the online version, at doi:10.1016/j.jmps.2019.103750.

References

Abel, A., 1987. Historical Perspectives and Some of the Main Features of the Bauschinger Effect, Materials Forum. Institute of Metals and Materials Australasia, pp. 11–26.
Ardeljan, M., Beyerlein, I.J., Knezevic, M., 2014. A dislocation density based crystal plasticity finite element model: application to a two-phase polycrystalline HCP/BCC composites. J. Mech. Phys. Solids 66, 16–31.
Ardeljan, M., Beyerlein, I.J., Knezevic, M., 2017. Effect of dislocation density-twin interactions on twin growth in AZ31 as revealed by explicit crystal plasticity finite element modeling. Int. J. Plast. 99, 81–101.
Ardeljan, M., Beyerlein, I.J., McWilliams, B.A., Knezevic, M., 2016. Strain rate and temperature sensitive multi-level crystal plasticity model for large plastic deformation behavior: application to AZ31 magnesium alloy. Int. J. Plast. 83, 90–109.
Ardeljan, M., Knezevic, M., 2018. Explicit modeling of double twinning in AZ31 using crystal plasticity finite elements for predicting the mechanical fields for twin variant selection and fracture analyses. Acta. Mater. 157, 339–354.
Ardeljan, M., Knezevic, M., Nizolek, T., Beyerlein, I.J., Mara, N.A., Pollock, T.M., 2015a. A study of microstructure-driven strain localizations in two-phase polycrystalline HCP/BCC composites using a multi-scale model. Int. J. Plast. 74, 35–57.
Ardeljan, M., Knezevic, M., Nizolek, T., Beyerlein, I.J., Zheng, S.J., Carpenter, J.S., McCabe, R.J., Mara, N.A., Pollock, T.M., 2014b. A multi-scale model for texture development in Zr/Nb nanolayered composites processed by accumulative roll bonding. IOP Conf. Ser.: Mater. Sci. Eng. 63, 012170.
Ardeljan, M., McCabe, R.J., Beyerlein, I.J., Knezevic, M., 2015b. Explicit incorporation of deformation twins into crystal plasticity finite element models. Comput. Methods Appl. Mech. Eng. 295, 396–413.
Asaro, R.J., Needleman, A., 1985. Texture development and strain hardening in rate dependent polycrystals. Acta Metall. Mater. 33, 923–953.
Barrett, T.J., Eghtesad, A., McCabe, R.J., Clausen, B., Brown, D.W., Vogel, S.C., Knezevic, M., 2019. A generalized spherical harmonics-based procedure for the interpolation of partial datasets of orientation distributions to enable crystal mechanics-based simulations. Materialia 6, 100328.
Barrett, T.J., Knezevic, M., 2019. Deep drawing simulations using the finite element method embedding a multi-level crystal plasticity constitutive law: experimental verification and sensitivity analysis. Comput. Methods Appl. Mech. Eng. 354, 245–270.
Barrett, T.J., Savage, D.J., Ardeljan, M., Knezevic, M., 2018. An automated procedure for geometry creation and finite element mesh generation: application to explicit grain structure models and machining distortion. Comput. Mater. Sci. 141, 269–281.
Barton, N., Bernier, J., Knap, J., Sunwoo, A., Cerreta, E., Turner, T., 2011. A call to arms for task parallelism in multi-scale materials modeling. Int. J. Numer. Methods Eng. 86, 744–764.
Bauschinger, J., 1886. Über die Veränderung der Elasticitätsgrenze und Festigkeit des Eisen und Stahls durch Strecken und Quetschen, durch Erwarmen und Abkühlen und durch oftmal wiederholte Beanspruchung. Mitteilungen aus dem mechanisch-technischen Laboratorium der k. polytechnischen Schule 1877-1836.
Bayley, C.J., Brekelmans, W.A.M., Geers, M.G.D., 2006. A comparison of dislocation induced back stress formulations in strain gradient crystal plasticity. Int. J. Solids Struct. 43, 7268–7286.
Bellman, R., Adomian, G., 1985. Green's Functions for Partial Differential Equations, Partial Differential Equations. Springer, pp. 243–247.
Berbenni, S., Favier, V., Lemoine, X., Berveiller, M., 2004. Micromechanical modeling of the elastic-viscoplastic behavior of polycrystalline steels having different microstructures. Mater. Sci. Eng. A 372 (1–2), 128–136.
Beyerlein, I.J., Tomé, C.N., 2008. A dislocation-based constitutive law for pure Zr including temperature effects. Int. J. Plast. 24, 867–895.
Bhargava, M., Chakrabarty, S., Barnwal, V.K., Tewari, A., Mishra, S.K., 2018. Effect of microstructure evolution during plastic deformation on the formability of Transformation Induced Plasticity and Quenched & Partitioned AHSS. Mater. Des. 152, 65–77.
Bhattacharyya, A., Knezevic, M., Abouaf, M., 2015. Characterization of crystallographic texture and intra-grain morphology in cross-rolled tantalum. Metall. Mater. Trans. A 46, 1085–1096.
Brown, L.M., Stobbs, W.M., 1971. The work-hardening of copper-silica: I. A model based on internal stresses, with no plastic relaxation. Philos. Mag. 23, 1185–1199.
Bunge, H.-J., 1993. Texture analysis in materials science. Mathematical Methods. Cuvillier Verlag, Göttingen.
Calcagnotto, M., Adachi, Y., Ponge, D., Raabe, D., 2011. Deformation and fracture mechanisms in fine- and ultrafine-grained ferrite/martensite dual-phase steels and the effect of aging. Acta. Mater. 59, 658–670.
Calcagnotto, M., Ponge, D., Raabe, D., 2012. Microstructure control during fabrication of ultrafine grained dual-phase steel: characterization and effect of intercritical annealing parameters. ISIJ Int. 52, 874–883.
Cantara, A.M., Zecevic, M., Eghtesad, A., Poulin, C.M., Knezevic, M., 2019. Predicting elastic anisotropy of dual-phase steels based on crystal mechanics and microstructure. Int. J. Mech. Sci. 151, 639–649.
Demir, E., Raabe, D., 2010. Mechanical and microstructural single-crystal Bauschinger effects: observation of reversible plasticity in copper during bending. Acta. Mater. 58, 6055–6063.
Deng, N., Korkolis, Y.P., 2018. Elastic anisotropy of dual-phase steels with varying martensite content. Int. J. Solids Struct. 141–142, 264–278.
Diehl, M., An, D., Shanthraj, P., Zaefferer, S., Roters, F., Raabe, D., 2017. Crystal plasticity study on stress and strain partitioning in a measured 3D dual phase steel microstructure. Phys. Mesomech. 20, 311–323.
EDAX, TSL, Manual for orientation imaging microscopy (OIM^{TM}), Version 7.1.0
Eghtesad, A., Barrett, T.J., Germaschewski, K., Lebensohn, R.A., McCabe, R.J., Knezevic, M., 2018a. OpenMP and MPI implementations of an elasto-viscoplastic fast Fourier transform-based micromechanical solver for fast crystal plasticity modeling. Adv. Eng. Softw. 126, 46–60.
Eghtesad, A., Barrett, T.J., Knezevic, M., 2018b. Compact reconstruction of orientation distributions using generalized spherical harmonics to advance large-scale crystal plasticity modeling: verification using cubic, hexagonal, and orthorhombic polycrystals. Acta Mater. 155, 418–432.
Eghtesad, A., Germaschewski, K., Lebensohn, R.A., Knezevic, M., 2019. A multi-GPU implementation of a full-field crystal plasticity solver for efficient modeling of high-resolution microstructures. Comput. Phys. Commun..
Eghtesad, A., Zecevic, M., Lebensohn, R.A., McCabe, R.J., Knezevic, M., 2018c. Spectral database constitutive representation within a spectral micromechanical solver for computationally efficient polycrystal plasticity modelling. Comput. Mech. 61, 89–104.

Evers, L.P., Brekelmans, W.A.M., Geers, M.G.D., 2004. Non-local crystal plasticity model with intrinsic SSD and GND effects. J. Mech. Phys. Solids 52, 2379–2401.
Feather, W.G., Ghorbanpour, S., Savage, D.J., Ardeljan, M., Jahedi, M., McWilliams, B.A., Gupta, N., Xiang, C., Vogel, S.C., Knezevic, M., 2019. Mechanical response, twinning, and texture evolution of WE43 magnesium-rare earth alloy as a function of strain rate: experiments and multi-level crystal plasticity modeling. Int. J. Plast. 120, 180–204.
Fleck, N.A., Muller, G.M., Ashby, M.F., Hutchinson, J.W., 1994. Strain gradient plasticity: theory and experiment. Acta Metall. Mater. 42, 475–487.
Gardey, B., Bouvier, S., Bacroix, B., 2005. Correlation between the macroscopic behavior and the microstructural evolutions during large plastic deformation of a dual-phase steel. Metall. Mater. Trans. A 36, 2937–2945.
Ghaei, A., Green, D.E., Aryanpour, A., 2015. Springback simulation of advanced high strength steels considering nonlinear elastic unloading–reloading behavior. Mater. Des. 88, 461–470.
Ghorbanpour, S., Zecevic, M., Kumar, A., Jahedi, M., Bicknell, J., Jorgensen, L., Beyerlein, I.J., Knezevic, M., 2017. A crystal plasticity model incorporating the effects of precipitates in superalloys: application to tensile, compressive, and cyclic deformation of Inconel 718. Int. J. Plast. 99, 162–185.
Gong, H., Wang, S., Knysh, P., Korkolis, Y.P., 2016. Experimental investigation of the mechanical response of laser-welded dissimilar blanks from advanced- and ultra-high-strength steels. Mater. Des. 90, 1115–1123.
Groeber, M.A., Jackson, M.A., 2014. DREAM. 3D: a digital representation environment for the analysis of microstructure in 3D. Integr. Mater. Manuf. Innov. 3, 5.
Hasegawa, T., Yakou, T., Karashima, S., 1975. Deformation behaviour and dislocation structures upon stress reversal in polycrystalline aluminium. Mater. Sci. Eng. 20, 267–276.
Hutchinson, J.W., 1976. Bounds and self-consistent estimates for creep of polycrystalline materials. Proc. R. Soc. Lond. Ser. A Math. Phys. Sci. 348, 101–126.
Jahedi, M., Ardjmand, E., Knezevic, M., 2017. Microstructure metrics for quantitative assessment of particle size and dispersion: application to metal-matrix composites. Powder Technol. 311, 226–238.
Jahedi, M., Paydar, M.H., Zheng, S., Beyerlein, I.J., Knezevic, M., 2014. Texture evolution and enhanced grain refinement under high-pressure-double-torsion. Mater. Sci. Eng. A 611, 29–36.
Kadkhodapour, J., Schmauder, S., Raabe, D., Ziaei-Rad, S., Weber, U., Calcagnotto, M., 2011. Experimental and numerical study on geometrically necessary dislocations and non-homogeneous mechanical properties of the ferrite phase in dual phase steels. Acta Mater. 59, 4387–4394.
Kapp, M., Hebesberger, T., Kolednik, O., 2011. A micro-level strain analysis of a high-strength dual-phase steel. Int. J. Mater. Res. 102, 687–691.
Kim, J.H., Kim, D., Barlat, F., Lee, M.-G., 2012. Crystal plasticity approach for predicting the Bauschinger effect in dual-phase steels. Mater. Sci. Eng. 539, 259–270.
Kitayama, K., Tomé, C., Rauch, E., Gracio, J., Barlat, F., 2013. A crystallographic dislocation model for describing hardening of polycrystals during strain path changes. Application to low carbon steels. Int. J. Plast. 46, 54–69.
Knezevic, M., Beyerlein, I.J., Brown, D.W., Sisneros, T.A., Tomé, C.N., 2013a. A polycrystal plasticity model for predicting mechanical response and texture evolution during strain-path changes: application to beryllium. Int. J. Plast. 49, 185–198.
Knezevic, M., Beyerlein, I.J., Lovato, M.L., Tomé, C.N., Richards, A.W., McCabe, R.J., 2014a. A strain-rate and temperature dependent constitutive model for BCC metals incorporating non-Schmid effects: application to tantalum–tungsten alloys. Int. J. Plast. 62, 93–104.
Knezevic, M., Capolungo, L., Tomé, C.N., Lebensohn, R.A., Alexander, D.J., Mihaila, B., McCabe, R.J., 2012. Anisotropic stress–strain response and microstructure evolution of textured α-uranium. Acta Mater. 60, 702–715.
Knezevic, M., Drach, B., Ardeljan, M., Beyerlein, I.J., 2014b. Three dimensional predictions of grain scale plasticity and grain boundaries using crystal plasticity finite element models. Comput. Methods Appl. Mech. Eng. 277, 239–259.
Knezevic, M., Landry, N.W., 2015. Procedures for reducing large datasets of crystal orientations using generalized spherical harmonics. Mech. Mater. 88, 73–86.
Knezevic, M., McCabe, R.J., Lebensohn, R.A., Tomé, C.N., Liu, C., Lovato, M.L., Mihaila, B., 2013b. Integration of self-consistent polycrystal plasticity with dislocation density based hardening laws within an implicit finite element framework: application to low-symmetry metals. J. Mech. Phys. Solids 61, 2034–2046.
Knezevic, M., McCabe, R.J., Tomé, C.N., Lebensohn, R.A., Chen, S.R., Cady, C.M., Gray Iii, G.T., Mihaila, B., 2013c. Modeling mechanical response and texture evolution of α-uranium as a function of strain rate and temperature using polycrystal plasticity. Int. J. Plast. 43, 70–84.
Knezevic, M., Nizolek, T., Ardeljan, M., Beyerlein, I.J., Mara, N.A., Pollock, T.M., 2014c. Texture evolution in two-phase Zr/Nb lamellar composites during accumulative roll bonding. Int. J. Plast. 57, 16–28.
Knezevic, M., Savage, D.J., 2014. A high-performance computational framework for fast crystal plasticity simulations. Comput. Mater. Sci. 83, 101–106.
Knezevic, M., Zecevic, M., Beyerlein, I.J., Bhattacharyya, A., McCabe, R.J., 2015a. Predicting texture evolution in Ta and Ta-10 W Alloys using polycrystal plasticity. JOM 67, 2670–2674.
Knezevic, M., Zecevic, M., Beyerlein, I.J., Bingert, J.F., McCabe, R.J., 2015b. Strain rate and temperature effects on the selection of primary and secondary slip and twinning systems in HCP Zr. Acta Mater. 88, 55–73.
Kocks, U.F., Tomé, C.N., Wenk, H.-.R., 1998. Texture and Anisotropy. Cambridge University Press, Cambridge, UK.
Lavrentev, F.F., 1980. The type of dislocation interaction as the factor determining work hardening. Mater. Sci. Eng. 46, 191–208.
Lebensohn, R.A., 2001. N-site modeling of a 3D viscoplastic polycrystal using fast Fourier transform. Acta Mater. 49, 2723–2737.
Lebensohn, R.A., Kanjarla, A.K., Eisenlohr, P., 2012. An elasto-viscoplastic formulation based on fast Fourier transforms for the prediction of micromechanical fields in polycrystalline materials. Int. J. Plast. 32–33, 59–69.
Lebensohn, R.A., Needleman, A., 2016. Numerical implementation of non-local polycrystal plasticity using fast Fourier transforms. J. Mech. Phys. Solids 97, 333–351.
Lentz, M., Klaus, M., Beyerlein, I.J., Zecevic, M., Reimers, W., Knezevic, M., 2015a. In situ X-ray diffraction and crystal plasticity modeling of the deformation behavior of extruded Mg–Li–(Al) alloys: an uncommon tension–compression asymmetry. Acta Mater. 86, 254–268.
Lentz, M., Klaus, M., Wagner, M., Fahrenson, C., Beyerlein, I.J., Zecevic, M., Reimers, W., Knezevic, M., 2015b. Effect of age hardening on the deformation behavior of an Mg–Y–Nd alloy: in-situ X-ray diffraction and crystal plasticity modeling. Mater. Sci. Eng. 628, 396–409.
Liu, B., Raabe, D., Roters, F., Eisenlohr, P., Lebensohn, R.A., 2010. Comparison of finite element and fast Fourier transform crystal plasticity solvers for texture prediction. Model. Simul. Mater. Sci. Eng. 18, 085005.
Lücke, K., Hölscher, M., 1991. Rolling and recrystallization textures of BCC steels. Texture Stress Microstruct. 14, 585–596.
Ma, B., Liu, Z.G., Jiang, Z., Wu, X., Diao, K., Wan, M., 2016. Prediction of forming limit in DP590 steel sheet forming: an extended fracture criterion. Mater. Des. 96, 401–408.
Madec, R., Devincre, B., Kubin, L., Hoc, T., Rodney, D.J.S., 2003. The role of collinear interaction in dislocation-induced hardening. Science 301, 1879–1882.
Mecking, H., Kocks, U.F., 1981. Kinetics of flow and strain-hardening. Acta Metall. Mater. 29, 1865–1875.
Michel, J., Moulinec, H., Suquet, P., 2001. A computational scheme for linear and non-linear composites with arbitrary phase contrast. Int. J. Numer. Methods Eng. 52, 139–160.
Mompiou, F., Caillard, D., Legros, M., Mughrabi, H., 2012. In situ TEM observations of reverse dislocation motion upon unloading in tensile-deformed UFG aluminium. Acta Mater. 60, 3402–3414.
Mughrabi, H., 1983. Dislocation wall and cell structures and long-range internal stresses in deformed metal crystals. Acta Metall. 31, 1367–1379.
Mughrabi, H., 2001. On the role of strain gradients and long-range internal stresses in the composite model of crystal plasticity. Mater. Sci. Eng. 317, 171–180.
Nesterova, E.V., Bouvier, S., Bacroix, B., 2015. Microstructure evolution and mechanical behavior of a high strength dual-phase steel under monotonic loading. Mater. Charact. 100, 152–162.

Ohno, N., 1982. A constitutive model of cyclic plasticity with a nonhardening strain region. J. Appl. Mech. 49 (4), 721–727.
Ohno, N., Kachi, Y., 1986. A constitutive model of cyclic plasticity for nonlinear hardening materials. J. Appl. Mech. 53 (2), 395–403.
Poulin, C.M., Korkolis, Y.P., Kinsey, B.L., Knezevic, M., 2019. Over five-times improved elongation-to-fracture of dual-phase 1180 steel by continuous-bending-under-tension. Mater. Des. 161, 95–105.
Ramazani, A., Mukherjee, K., Schwedt, A., Goravanchi, P., Prahl, U., Bleck, W., 2013. Quantification of the effect of transformation-induced geometrically necessary dislocations on the flow-curve modelling of dual-phase steels. Int. J. Plast. 43, 128–152.
Randle, V., Engler, O., 2000. Introduction to texture analysis. Macrotexture, Microstructure & Orientation Mapping. Gordon and Breach Science Publishers.
Ray, R., Jonas, J.J., Hook, R., 1994. Cold rolling and annealing textures in low carbon and extra low carbon steels. Int. Mater. Rev. 39, 129–172.
Rocha, R.O., Melo, T.M.F., Pereloma, E.V., Santos, D.B., 2005. Microstructural evolution at the initial stages of continuous annealing of cold rolled dual-phase steel. Mater. Sci. Eng. A 391, 296–304.
Sakaki, T., Sugimoto, K., Fukuzato, T., 1983. Role of internal stress for continuous yielding of dual-phase steels. Acta Metall. 31, 1737–1746.
Savage, D.J., Knezevic, M., 2015. Computer implementations of iterative and non-iterative crystal plasticity solvers on high performance graphics hardware. Comput. Mech. 56, 677–690.
Schemmann, L., Zaefferer, S., Raabe, D., Friedel, F., Mattissen, D., 2015. Alloying effects on microstructure formation of dual phase steels. Acta Mater. 95, 386–398.
Smith, D.H., Bicknell, J., Jorgensen, L., Patterson, B.M., Cordes, N.L., Tsukrov, I., Knezevic, M., 2016. Microstructure and mechanical behavior of direct metal laser sintered Inconel alloy 718. Mater. Charact. 113, 1–9.
Sritharan, T., Chandel, R.S., 1997. Phenomena in interrupted tensile tests of heat treated aluminium alloy 6061. Acta Mater. 45, 3155–3161.
Stout, M., Rollett, A., 1990. Large-strain Bauschinger effects in FCC metals and alloys. Metall. Mater. Trans. A 21, 3201–3213.
Sumikawa, S., Ishiwatari, A., Hiramoto, J., Urabe, T., 2016. Improvement of springback prediction accuracy using material model considering elastoplastic anisotropy and Bauschinger effect. J. Mater. Process. Technol. 230, 1–7.
Tasan, C.C., Diehl, M., Yan, D., Bechtold, M., Roters, F., Schemmann, L., Zheng, C., Peranio, N., Ponge, D., Koyama, M., Tsuzaki, K., Raabe, D., 2015. An overview of dual-phase steels: advances in microstructure-oriented processing and micromechanically guided design. Annu. Rev. Mater. Res. 45, 391–431.
Tasan, C.C., Hoefnagels, J.P.M., Diehl, M., Yan, D., Roters, F., Raabe, D., 2014. Strain localization and damage in dual phase steels investigated by coupled in-situ deformation experiments and crystal plasticity simulations. Int. J. Plast. 63, 198–210.
Verma, R.K., Kuwabara, T., Chung, K., Haldar, A., 2011. Experimental evaluation and constitutive modeling of non-proportional deformation for asymmetric steels. Int. J. Plast. 27, 82–101.
Von Schlippenbach, U., Emren, F., Lücke, K., 1986. Investigation of the development of the cold rolling texture in deep drawing steels by ODF-analysis. Acta Metall. 34, 1289–1301.
Wagoner, R.H., Lim, H., Lee, M.-G., 2013. Advanced issues in springback. Int. J. Plast. 45, 3–20.
Wen, W., Borodachenkova, M., Tomé, C., Vincze, G., Rauch, E., Barlat, F., Grácio, J., 2015. Mechanical behavior of Mg subjected to strain path changes: experiments and modeling. Int. J. Plast. 73, 171–183.
Wilson, D.V., Bate, P.S., 1986. Reversibility in the work hardening of spheroidised steels. Acta Metall. 34, 1107–1120.
Wilson, D.V., Zandrahimi, M., Roberts, W.T., 1990. Effects of changes in strain path on work-hardening in CP aluminium and an Al–Cu–Mg alloy. Acta Metall. Mater. 38, 215–226.
Withers, P., Bhadeshia, H., 2001. Residual stress. Part 1 – measurement techniques. Mater. Sci. Technol. 17, 355–365.
Woo, W., Em, V.T., Kim, E.Y., Han, S.H., Han, Y.S., Choi, S.H., 2012. Stress–strain relationship between ferrite and martensite in a dual-phase steel studied by in situ neutron diffraction and crystal plasticity theories. Acta Mater. 60, 6972–6981.
Yoshida, F., Uemori, T., Fujiwara, K., 2002. Elastic–plastic behavior of steel sheets under in-plane cyclic tension–compression at large strain. Int. J. Plast. 18, 633–659.
Yoshida, K., Brenner, R., Bacroix, B., Bouvier, S., 2011. Micromechanical modeling of the work-hardening behavior of single-and dual-phase steels under two-stage loading paths. Mater. Sci. Eng. 528, 1037–1046.
Zayed, A.I., 1998. A convolution and product theorem for the fractional Fourier transform. IEEE Signal Process. Lett. 5, 101–103.
Zecevic, M., Knezevic, M., 2015. A dislocation density based elasto-plastic self-consistent model for the prediction of cyclic deformation: application to Al6022-T4. Int. J. Plast. 72, 200–217.
Zecevic, M., Knezevic, M., 2018a. Latent hardening within the elasto-plastic self-consistent polycrystal homogenization to enable the prediction of anisotropy of AA6022-T4 sheets. Int. J. Plast. 105, 141–163.
Zecevic, M., Knezevic, M., 2018b. A new visco-plastic self-consistent formulation implicit in dislocation-based hardening within implicit finite elements: application to high strain rate and impact deformation of tantalum. Comput. Methods Appl. Mech. Eng. 341, 888–916.
Zecevic, M., Knezevic, M., 2019. An implicit formulation of the elasto-plastic self-consistent polycrystal plasticity model and its implementation in implicit finite elements. Mech. Mater. 136, 103065.
Zecevic, M., Knezevic, M., Beyerlein, I.J., McCabe, R.J., 2016a. Origin of texture development in orthorhombic uranium. Mater. Sci. Eng. A 665, 108–124.
Zecevic, M., Knezevic, M., Beyerlein, I.J., McCabe, R.J., 2016b. Texture formation in orthorhombic alpha-uranium under simple compression and rolling to high strains. J. Nucl. Mater. 473, 143–156.
Zecevic, M., Knezevic, M., Beyerlein, I.J., Tomé, C.N., 2015. An elasto-plastic self-consistent model with hardening based on dislocation density, twinning and de-twinning: application to strain path changes in HCP metals. Mater. Sci. Eng. A 638, 262–274.
Zecevic, M., Korkolis, Y.P., Kuwabara, T., Knezevic, M., 2016c. Dual-phase steel sheets under cyclic tension–compression to large strains: experiments and crystal plasticity modeling. J. Mech. Phys. Solids 96, 65–87.